Re-energization of AGN head–tail radio galaxies in the galaxy cluster ZwCl 0634.1+47474

G. Lusetti [1]★ F. de Gasperin [1,2]★ V. Cuciti,[1,2] M. Brüggen [1] C. Spinelli,[3] H. Edler,[1] G. Brunetti,[2] R. J. van Weeren,[4] A. Botteon [2] G. Di Gennaro [1] R. Cassano,[2] C. Tasse[6,7] and T. W. Shimwell[4,5]

[1]*Hamburger Sternwarte, Universität Hamburg, Gojenbergsweg 112, D-21029 Hamburg, Germany*
[2]*INAF - Istituto di Radioastronomia di Bologna, Via Gobetti 101, I-40129 Bologna, Italy*
[3]*Argelander-Institut für Astronomie Universitäat Bonn, Auf dem Hğel 71, D-53121 Bonn, Germany*
[4]*Leiden Observatory, Leiden University, PO Box 9513, NL-2300 RA Leiden, The Netherlands*
[5]*ASTRON, The Netherlands Institute for Radio Astronomy, Oude Hoogeveensedijk 4, NL-7991 PD, Dwingeloo, The Netherlands*
[6]*GEPI, Observatoire de Paris, CNRS, Université Paris Diderot, 5 place Jules Janssen, F-92190 Meudon, France*
[7]*Department of Physics and Electronics, Centre for Radio Astronomy Techniques and Technologies, Rhodes University, Grahamstown 6140, South Africa*

ABSTRACT
Low-frequency radio observations show an increasing number of radio galaxies located in galaxy clusters that display peculiar morphologies and spectral profiles. This is the result of the dynamical interaction of the galaxy with the surrounding medium. Studying this phenomenon is key to understanding the evolution of low-energy relativistic particles in the intracluster medium. We present a multifrequency study of the three head–tail (HT) radio galaxies and the radio halo in the galaxy cluster ZwCl 0634.1+4747. We make use of observations at four frequencies performed with LOFAR LBA (53 MHz), HBA (144 MHz), GMRT (323 MHz), and VLA (1518 MHz) data. The use of extremely low radio frequency observations, such as LOFAR at 53 and 144 MHz, allowed us to detect the extension of the tails up to a distance of ∼1 Mpc. We extracted spectral profiles along the tails in order to identify possible departures from a pure ageing model, such as the Jaffe–Perola (JP) model, which only involves synchrotron and inverse-Compton losses. We found clear evidence of departures from this simple ageing model, such as surface brightness enhancement and spectral flattening along all of the tails. This can be interpreted as the consequence of particle re-acceleration along the tails. Possible explanations for this behaviour include the interaction between a shock and the radio tails or a turbulence-driven re-acceleration mechanism. We show that the latter scenario is able to reproduce the characteristic features that we observed in our profiles.

Key words: galaxies: clusters: general – radio continuum: galaxies – radio continuum: ISM.

1 INTRODUCTION

Galaxy clusters host a large variety of radio emission, generally divided between diffuse radio sources (van Weeren et al. 2019) and radio galaxies (Hardcastle & Croston 2020). These non-thermal emissions are the results of relativistic cosmic ray electrons (CRe) interacting with the cluster or galactic magnetic field.

Radio galaxies in clusters of galaxies usually show distorted morphologies (O'Dea & Owen 1985; Feretti & Giovannini 2008; Garon et al. 2019), because of the dynamical interaction between the radio jets and the surrounding dense ($n_e \sim 10^{-2} - 10^{-4}$ cm^{-3}), hot ($10^7 - 10^9$ K) intracluster medium (ICM). The first morphological classification by Owen & Rudnick (1976) is based on the angle between the radio tails and the core of the galaxy (see also Miley 1980, for a review). Narrow-angle tails (NATs; Venkatesan et al. 1994; Feretti et al. 1998) have angles between the two jets smaller

than 90°, because of the high ram pressure they experience that leads to the narrow V- or L-shape they assume. Wide-angle tails (WATs; Klamer, Subrahmanyan & Hunstead 2004; Mao et al. 2010) show C-type morphologies with angles between the two tails greater than 90° but smaller than 180°. They are usually thought to experience weaker ram pressure, caused by low velocities relative to the cluster centre and/or lower density of the surrounding ICM. Among these types, we focus on the head–tail (HT) radio galaxies (Ryle & Windram 1968; Hill & Longair 1971; Miley 1973; Sebastian, Lal & Pramesh Rao 2017; Cuciti et al. 2018; Lal 2020; Srivastava & Singal 2020; Botteon et al. 2021; Müller et al. 2021), NATs whose distinctive feature is a very elongated structure formed by the radio jets. In HT radio galaxies, both jets are bent in the same direction and thus it is not always possible to resolve them. Their radio surface brightness usually peaks close to the host (optical) galaxy and gradually decreases along the tail that can reach up to hundreds of kiloparsecs (e.g. Srivastava & Singal 2020; Botteon et al. 2021). Their spectral index becomes steeper, moving from the core towards the tail (e.g. Cuciti et al. 2018; Wilber et al. 2018), while the fractional

★ E-mail: giulia.lusetti@hs.uni-hamburg.de (GL); fdg@ira.inaf.it (FdG)

polarisation increases along the jets (Feretti et al. 1998; Müller et al. 2021), reflecting an increase of the degree of ordering of the magnetic field. However, after the jets are launched into the ICM, relativistic electrons are visible only for tens of Myrs at GHz frequencies because of their energy losses, owing to synchrotron and Inverse-Compton (IC) emission. Thus, these tails left behind by the galaxy moving within the cluster are expected to fade quickly, becoming invisible at high frequencies. Because of the longer cooling times of low-energy CRe, low-frequency observations are crucial for identifying and tracing CRe for much longer.

In fact, with the advent of low-frequency (<1 GHz) radio astronomy, tails extending to very long distances have become more common and can be studied in detail (Sebastian, Lal & Pramesh Rao 2017; de Gasperin 2017; Wilber et al. 2018; Botteon et al. 2021; Edler et al. 2022). In this context, the LOw-Frequency Array (LOFAR; van Haarlem et al. 2013a), being the largest and most sensitive radio-interferometer in the 10–240 MHz regime, has made many recent contributions to the field (e.g. Mandal et al. 2020; Pal & Kumari 2023).

Moreover, in some cases the tails show peculiar properties, such as an increase in surface brightness and flattening of the spectral index along the tail (e.g. Sijbring & de Bruyn 1998; Parma et al. 1999; Giacintucci et al. 2007; de Gasperin 2017). To explain such behaviours far from the host galaxy, the presence of re-energetization processes has been proposed. In fact, re-acceleration of CRe would be able to power the population of aged electrons initially injected by the AGN, making them visible at larger distances, where they would be expected to disappear owing to radiative losses. For example, de Gasperin (2017) proposed a re-acceleration mechanism invoking turbulence driven into the tail by interactions with the ICM. This would create the so-called gently re-energized tail (GReET; de Gasperin 2017; Edler et al. 2022) sources. Müller et al. (2021) suggest the transition from laminar to turbulent flow as the cause of gentle re-acceleration of the electrons along the tail. They also point out that for complex morphologies, more than one AGN cycle, that is, a change in the injection rate, must be taken into account to explain the entire appearance of the jets. In other cases, adiabatic compression (Enßlin & Gopal-Krishna 2001; Enßlin & Brüggen 2002) would be able to form radio phoenices, revived fossil plasma from old radio lobes. Radio phoenices usually show an irregular morphology, steep spectral index ($\alpha \sim < -1.5$ with the $S_\nu \propto \nu^\alpha$ for the synchrotron emission) and curved integrated spectra (Kempner et al. 2004; van Weeren et al. 2009; van Weeren, Röttgering & Brüggen 2011; de Gasperin et al. 2015; Mandal et al. 2019; Duchesne, Johnston-Hollitt & Bartalucci 2021; Pasini et al. 2022). A first attempt to systematically study radio phoenices was performed by Mandal et al. (2020). They found a non-uniform spectral index across the sources, suggesting a possible mix of cosmic ray populations with different ages, losses, and re-acceleration efficiencies. Regardless of the type of mechanism that generates them, sources that trace re-energized AGN radio plasma are characterized by very steep spectra. Thus, low-frequency facilities, such as LOFAR, are ideal to study these phenomena.

An increasing number of galaxy clusters is also observed to host diffuse Mpc-scale sources, called radio haloes (see van Weeren et al. 2019, for a review). Radio haloes are steep spectrum ($\alpha < -1.1$), centrally located sources, whose morphology roughly follows the distribution of the thermal ICM. Turbulent re-acceleration is thought to be the main mechanism responsible for generating radio haloes (see e.g. Brunetti & Jones 2014). In this scenario, a population of seed particles are re-accelerated by turbulence generated in the ICM during cluster mergers. Thus, the presence of radio haloes is
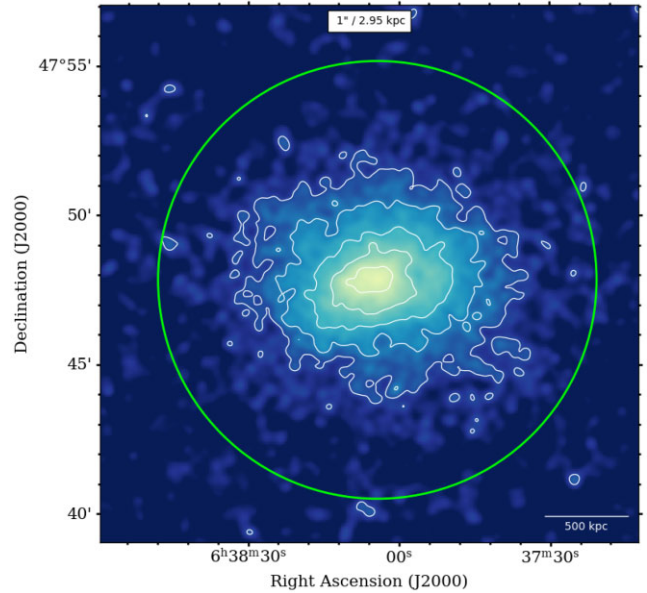
Figure 1. Background-subtracted exposure-corrected XMM image of ZwCl 0634.1+4747, in [0.5–2] keV band. The contour levels start at $3 \cdot$ rms where rms $= 5 \cdot 10^{-6}$ cts s^{-1}. As a size reference, green circle indicates $R_{500} = 1299$ kpc (Lovisari et al. 2017), namely the radius within which the mean mass over-density of the cluster is 500 times the cosmic critical density at the cluster redshift.

connected to the merging history of the systems and the cluster mass, which sets the available energy budget during mergers. Observational evidences for this scenario are the connection between the dynamical status of the cluster and the presence of radio haloes (Buote 2001; Cassano et al. 2010; Cuciti et al. 2015, 2021) and the correlation between radio haloes power and the mass of the host cluster (Cassano et al. 2013; Cuciti et al. 2021; Duchesne, Johnston-Hollitt & Bartalucci 2021; van Weeren et al. 2021; Cuciti et al. 2023). A key prediction of the turbulent re-acceleration model is that the cutoff in the synchrotron spectrum scales with the energetics of the merger (e.g. Cassano & Brunetti 2005; Cassano, Brunetti & Setti 2006). This means that more massive systems suffering major mergers, host radio haloes visible up to ∼GHz frequencies, while less massive systems and/or minor mergers produce radio haloes with steeper spectra ($\alpha < -1.5$), preferentially detectable at lower frequencies. These are generally referred to as Ultra-Steep Spectrum radio haloes (USSRHs; Brunetti et al. 2008).

1.1 ZwCl 0634.1+4747

ZwCl 0634.1+4747 is a massive ($M_{500} = (6.65 \pm 0.33) \times 10^{14}$ M$_\odot$, Planck Collaboration et al. (2016)) nearby ($z = 0.174$, Rossetti et al. (2017)) galaxy cluster located at R.A.(J2000) 06^{h}38^{m}02^s.5, DEC.(J2000) $+47°$ 47$'$ 23.8$''$, also known as PSZ1 G167.64+17.63/ PSZ2 G167.67+17.63, CIZA J0638.1+4747, MCXC J0638.1+4747, or RXC J0638.1+4747. *Chandra* X-ray observations show evidence of a non-relaxed dynamical state, such as the presence of substructures in the X-ray surface brightness distribution (Cuciti et al. 2015). The morphology of the cluster is elongated in the east–west direction (see Fig. 1).

ZwCl 0634.1+4747 hosts a variety of peculiar radio sources. A radio halo was already detected at 323 and 1518 MHz by Cuciti et al. (2018). It extends over ∼600 kpc in the E–W direction following the morphology of the X-ray emission of the cluster. More recently, a
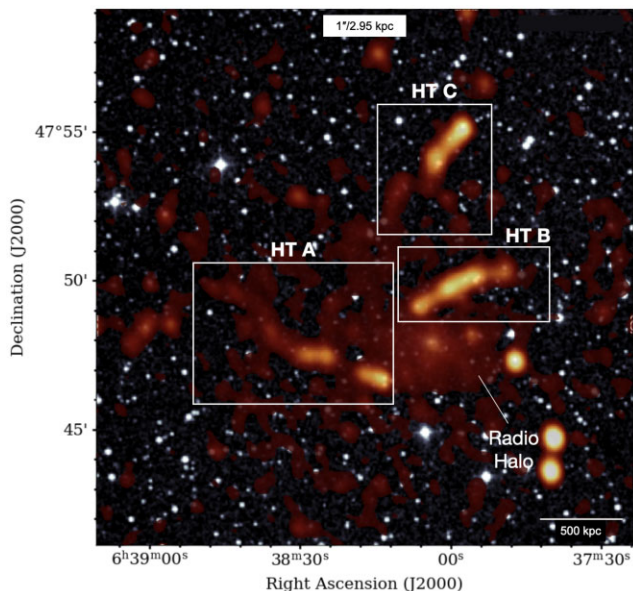
Figure 2. Composite radio-optical image of ZwCl 0634.1+4747. LOFAR HBA at 144 MHz superimposed on the DSS image (Pâris et al. 2014).

radio megahalo has been discovered in this system using LOFAR 144 MHz observations (Cuciti et al. 2022). The megahalo covers the whole cluster volume, with a linear size of 2.8 Mpc and an integrated spectral index between 53 and 144 MHz of $\alpha = -1.62 \pm 0.25$. In addition, LOFAR observations clearly revealed the presence of three HT radio galaxies in the cluster field, with $\sim 0.6 - 1$ Mpc linear size, labelled HT-A HT-B and HT-C in Fig. 2, which are the focus of this paper. The HT-B has been studied at high frequency (323 and 1518 MHz) by Cuciti et al. (2018). Possible signs of re-energetization have been found through the analysis of the spectral index and surface brightness along the tail. In that case, the interaction between the tail and a shock has been proposed to explain the emission.

In this paper we present a multiwavelength radio study of the galaxy cluster ZwCl 0634.1+4747, combining data from 53 MHz to 1.5 GHz. First, we focus our analysis on the three extended HT radio galaxies residing in ZwCl 0634.1+4747 (subsection 3.1). We produce flux density and spectral index profiles along the tails of the HT radio galaxies (subsection 3.1), comparing them with a standard ageing model (subsection 3.2). In subsection 3.3, we complement the analysis of the cluster with X-ray information using *XMM–Newton* data. Additionally, we present a new study of the radio halo down to the very-low frequencies in subsection 3.4. In Section 4, we discuss possible scenarios that involve the interaction of HT radio galaxies with the external ICM. We summarize our results in Section 5.

Throughout the paper we adopt a ΛCDM cosmology with $H_0 = 70 \, \mathrm{km \, s^{-1} Mpc^{-1}}$, $\Omega_\Lambda = 0.7$, and $\Omega_m = 0.3$. Thus, $1''$ cor-

responds to a physical scale of 2.95 kpc at the redshift of ZwCl 0634.1+4747. We use the convention $S_\nu \propto \nu^\alpha$ for the radio synchrotron emission, with $\alpha < 0$.

2 OBSERVATIONS AND DATA REDUCTION

The data used in this work cover a broad range of frequencies, including The LOFAR Low Band Antennas (LBA) at 53 MHz, High Band Antennas (HBA) at 144 MHz, Giant Meterwave Radio Telescope (GMRT) at 323 MHz and Karl G. Jansky Very Large Array (VLA) at 1.5 GHz data. A summary of the observations used is listed in Table 1. GMRT and VLA data of this cluster were already analysed by Cuciti et al. (2018), while LOFAR, LBA, and HBA data are extensively described is Cuciti et al. (2022). Thus, we briefly summarize the data-reduction procedure in further sections.

2.1 LOFAR LBA data

This cluster was observed at ultra-low frequencies using LOFAR LBA for a total of 8 h integration time in the frequency range 30–77 MHz, using the LBA_OUTER antenna configuration. Observations were conducted using the multibeam mode, with one beam continuously pointed at the calibrator and one beam at the target. First, following de Gasperin et al. (2019), the calibrator solutions are derived and applied to the target field together with the primary beam correction. The data of the target field were self-calibrated first for direction-independent, and then for direction-dependent effects (de Gasperin et al. 2020). Finally, the image quality was improved via extraction and self-calibration of a small region around the target, adapting the procedure used for HBA analysis of van Weeren et al. (2021) for LBA data. The final model and solutions from the direction-dependent calibration are used to subtract sources outside a circular region of $23'$ centred on the target. Then, the data set is phase-shifted to the centre of this region, corrected for the primary beam in this direction and additional rounds of self-calibration on the target are performed to further improve the image quality. For more details on the data used, we refer the reader to Cuciti et al. (2022), where the observations used in this work were first presented.

2.2 LOFAR HBA data

The LOFAR HBA data used in this work are part of the LOFAR Two-metre Sky Survey (LoTSS; Shimwell et al. 2017, 2019, 2022), a low-frequency (120–168 MHz) radio survey of the northern sky. Data were processed through the Survey Key Science Project reduction pipeline v2.2 presented in Tasse et al. (2021); Shimwell et al. (2022), which includes direction-independent and direction-dependent calibration (pre-factor (de Gasperin et al. 2019); killMS (Smirnov & Tasse 2015); DDFacet (Tasse et al. 2018)). Finally, the data sets have undergone the extraction procedure generally used for

Table 1. Observational overview: LOFAR LBA, HBA, GMRT, and VLA observation. References: (1) Cuciti et al. (2022), (2) Cuciti et al. (2018).

Telescope	Frequency MHz	Bandwidth MHz	Configuration	Time	Observation date	Reference
LOFAR LBA	53	47	LBA_OUTER	8 h	2018 Sep 28	(1)
LOFAR HBA	144	48	HBA_DUAL	8+8 h	2019 Oct 27, 2021 Mar 10	(1)
GMRT	320	32	-	5 h	2015 Dec 19	(2)
VLA L-band	1518	48	D array	45 min	2015 Oct 19	(2)
VLA L-band	1518	48	B array	40 min	2015 Feb 22	(2)

HBA observations to enhance the quality of the image (van Weeren et al. 2021; Botteon et al. 2022). For more details, we refer again to Cuciti et al. (2022), where the observations used in this work were firstly used.

A flux-scale correction factor $f = 0.992$ has been applied to the nominal LOFAR HBA map values to align the images with the flux density scale of the LoTSS (Hardcastle et al. 2021; Shimwell et al. 2022).

2.3 GMRT data

ZwCl 0634.1+4747 has been observed with the GMRT at 320 MHz for a total time on source of ∼5 h (Cuciti et al. 2018). First, amplitude and gain corrections were calculated for the calibrator sources and then transferred to the target. Radio frequency interference (RFI) has been removed automatically using Common Astronomy Software Applications package (CASA; McMullin et al. 2007) and the central 220 channels were averaged to 22 to reduce the size of the data set. Finally, a few steps of phase-only self-calibration were performed to reduce phase variations. Moreover, similarly to the extraction procedure, bright sources in the field of view were subtracted from the *uv*-data using the peeling method (see Cuciti et al. 2018, for more details on the data reduction of this data set).

2.4 VLA data

VLA L-band observations of ZwCl 0634.1+4747 include D and B array configuration with a total time on source of ∼45 and 40 min, respectively (Cuciti et al. 2018). First, the complex gain solutions for the calibrator sources (and the phase calibrator when present) on the full bandwidth were obtained, applying the bandpass and delay solution beforehand. Secondly, the calibration tables were applied to the target and an automatic RFI removal was made using CASA. The 48 central channels of each spectral window were averaged to 6 to reduce the size of the data set. All images were corrected for the primary beam attenuation.

After cycles of calibration and self-calibration on each array configuration, the B and D array observations were combined. Since the two pointings did not coincide perfectly, bright sources far from the phase centre are subtracted separately for each spectral window from the *uv*-data before combining the data set. The combined B+D array image is used for the HT analysis (subsection 3.1), while the D array only is used for imageing the extended radio halo (subsection 3.4).

2.5 Source subtraction

Discrete sources embedded in the extended radio halo, contaminate the diffuse emission and thus, we proceeded to remove them. This allows to properly study the low-surface brightness emission from the radio halo. Previous work (Cuciti et al. 2018, 2022) presented the source subtraction for the low-frequency (53 and 144 MHz) and high-frequency (323 and 1518 MHz) data set separately. To be consistent through our analysis, we apply the same source subtraction procedure for all four data sets. We describe here briefly the general process. First, we produced high (4″ × 5″) resolution images, to identify the compact sources. Secondly, we selected the corresponding components in the model image and we proceeded to remove them, subtracting these clean components directly from the *uv*−data. Finally, we imaged the source-subtracted data sets at low-angular resolution (see Fig. 3), maintaining a negative Briggs weighting with robust parameter −0.25, using a common inner *uv*-cut of 135λ (equivalent to an angular scale of ∼25′), which corresponds to the shortest baseline of the VLA data set. Moreover, we taper down the long baselines (i.e. using Gaussian taper with a FWHM of 30″) to gain sensitivity towards the diffuse emission.

Throughout the paper, the images were created with WSCLEAN software (Offringa et al. 2014). The uncertainty Δ_S associated with a flux density measurement S is estimated as

$$\Delta_S = \sqrt{(\sigma_c \cdot S)^2 + N_{beam} \cdot \sigma_{rms}^2}, \qquad (1)$$

where $N_{beam} = N_{pixel}/A_{beam}$ is the number of independent beams in the source area, and σ_c indicates the systematic calibration error on the flux density. Typical values of σ_c are within 10 per cent for LOFAR LBA (de Gasperin et al. 2021), HBA (Shimwell et al. 2022), and GMRT (e.g. Chandra, Ray & Bhatnagar 2004), while 2.5 per cent is used for VLA (Perley & Butler 2013).

2.6 *XMM–Newton* data

X-ray data for ZwCl 0634.1+4747are available in the *XMM–Newton* Science Archive (XSA), OBSID 0692932601. The data reduction of the *XMM–Newton* data is performed using HEASOFT version 6.29 (NASA High Energy Astrophysics Science Archive Research Centre (HEASARC) 2014) and the Science Analysis Software (SAS[1]) version 20.0.0. Hereafter, we provide a summary of the procedure. For a more extended description of the steps, the reader can refer to Veronica et al. (2022).

The first step consists of identifying Good Time Intervals (GTIs), filtering out those that are affected by the presence of soft proton flares (SPFs) (De Luca & Molendi 2004; Kuntz & Snowden 2008). This is achieved by creating a light curve for each of the three instruments of EPIC onboard of *XMM–Newton*, namely MOS1, MOS2, and pn. For all instruments, we also generate count histograms. In the absence of SPF contamination the histogram is well fitted by a Poisson distribution. This allows us to estimate a mean value for the counts and apply a $\pm 3\sigma$ cut to discard the time intervals affected by flares and, for this reason, falling outside this range. Additionally, the IN/OUT ratio test (De Luca & Molendi 2004; Leccardi & Molendi 2008) allows us to further check the quality of our flare filtering procedure by comparing the count rates within the FoV (IN) to those of the unexposed region of the detectors (OUT). An IN/OUT ratio close to 1 for each detector indicates that the contamination by SPF was successfully removed. After the SPF filtering procedure the exposure time is reduced from ∼21 to ∼13 ks for the MOS cameras and from ∼18 to ∼10 ks for pn. Note that MOS1-3 and MOS1-6 were not in use at the time of this observation. Moreover we model and rescale the instrumental background, eventually we subtract it to the observation of ZwCl 0634.1+4747and obtain background-subtracted and exposure-corrected images (Fig. 1). The procedure for this step is extensively described in Ramos-Ceja et al. (2019) and Migkas et al. (2020).

Since we are interested in the diffuse X-ray emission associated with the ICM in ZwCl 0634.1+4747, we mask the point sources that contaminate the field of view. First, we apply an automated procedure described in Pacaud et al. (2006) which detects point sources and stores them in a catalogue. Secondly, we manually remove any further sources by looking at images in the soft (0.5–2 keV) and hard (2–10 keV) X-ray bands. The surface brightness analysis, described in subsection 3.3, is performed on the masked images.
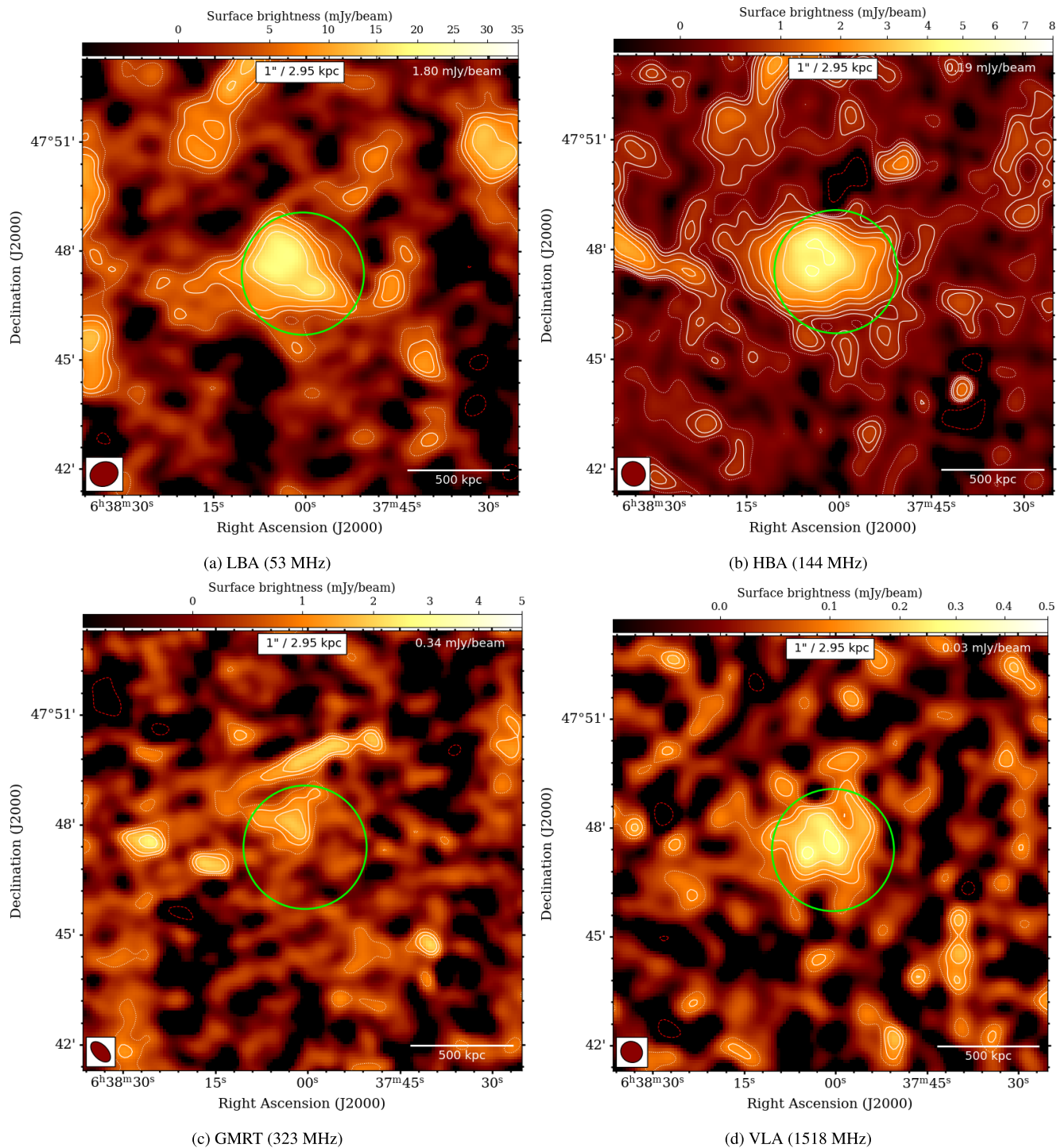
---

[1] https://www.cosmos.esa.int/web/xmm-newton/sas

(a) LBA (53 MHz)

(b) HBA (144 MHz)

(c) GMRT (323 MHz)

(d) VLA (1518 MHz)

Figure 3. Low-resolution source-subtracted images of the radio halo hosted by ZwCl 0634.1+4747. The beam is shown in the bottom left corner of each image. The contour levels start at $2\sigma_{\rm rms}$ (where $\sigma_{\rm rms}$ is shown in the top right area of the images) and are spaced with a factor of $\sqrt{2}$. The $2\sigma_{\rm rms}$ contours are dotted in white. The $-3\sigma_{\rm rms}$ contours are dashed in red colour. The green circle indicates the region with $R = 300$ kpc used to extract the flux densities (Table 4).

3 RESULTS

3.1 HT galaxies

The three HT galaxies in ZwCl 0634.1+4747 are all very extended and bright at lower frequencies (reaching up to ∼1 Mpc projected size at 144 MHz). They are spread over the cluster volume and show peculiar spectral properties. We named them HT-A, HT-B, and HT-C (see Fig. 2). Their properties, including the position and redshift of the optical counterpart, the projected distance from the cluster centre and their maximum extension measured from the $3\sigma_{\rm rms}$ contours of the LOFAR HBA image, are listed in Table 3. The cluster-centric distances are projected, and are thus lower limits. Wide-field, medium-resolution images are shown in Fig. 4 while
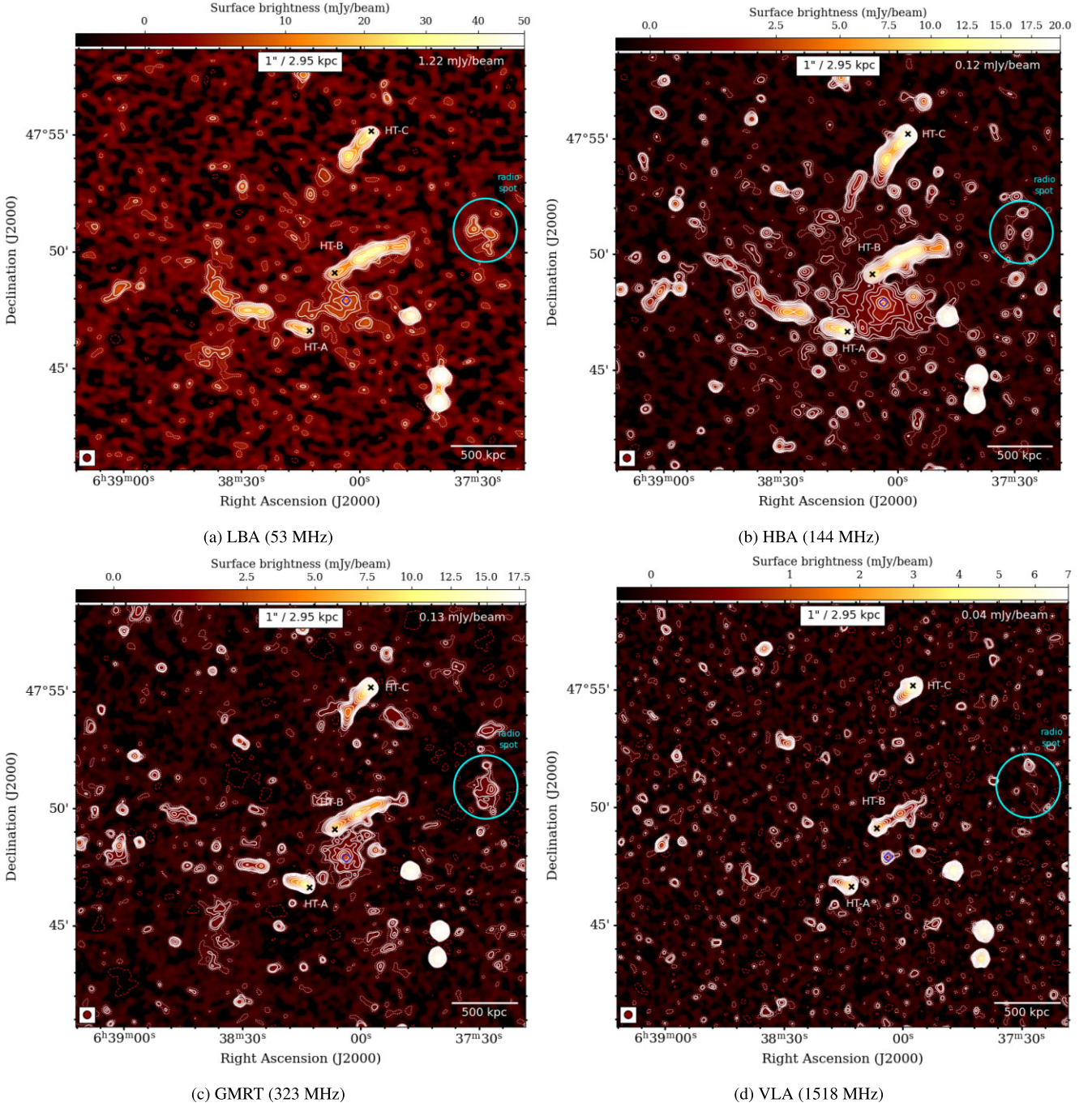
Figure 4. Images of the HT galaxies hosted in ZwCl 0634.1+4747at different frequencies. In each image, the contour levels start at $2\sigma_{rms}$, where σ_{rms} shown in the top right area of the images, and are spaced with a factor of $\sqrt{2}$. The $2\sigma_{rms}$ are dotted white coloured and $-3\sigma_{rms}$ contours are dashed red coloured. The beam is shown in the bottom left corner of each image and has a FWHM of $20''$. Black crosses indicate the optical counterparts of the HT radio galaxies (Table 3). The blue diamond is the location of the Brightest Cluster Galaxy (BCG) (Cutri et al. 2003).

zoomed-in images in Fig. 5. The locations of the optical counterparts are shown in Fig. 4. Photometric redshift are taken from the DESI DR9 photometric redshift catalogue (Zhou et al. 2021).

Every tail shows a bright head, followed by a lower surface brightness tail, which shows ripples in the radio brightness. The presence of multiple radio bumps could be interpreted as other radio-galaxies within the cluster volume rather than a continuation of the tails. In order to exclude the possibility of a sequence of multiple radio galaxies, we produced spectral index map between 53 and

144 MHz (Fig. 6, left) and 144–320 MHz (Fig. 6, right). To this end, we re-imaged LBA and HBA data, using Briggs weighting with Robust parameter $R = -0.25$, common uv-range and convolved to the same beam size. In each map, we measured spectral index values for pixels with flux density $\geq 2\sigma_{rms}$ in both frequencies. We find that $\alpha_{53\,MHz}^{144\,MHz}$ has flatter values where the heads of the AGN are located (consistent with values Fig. 7) and steepens along the tails. Hence, the bright bumps are unlike other AGN which are expected to have $\alpha \sim -0.5$. Moreover, no other optical counterparts at the cluster
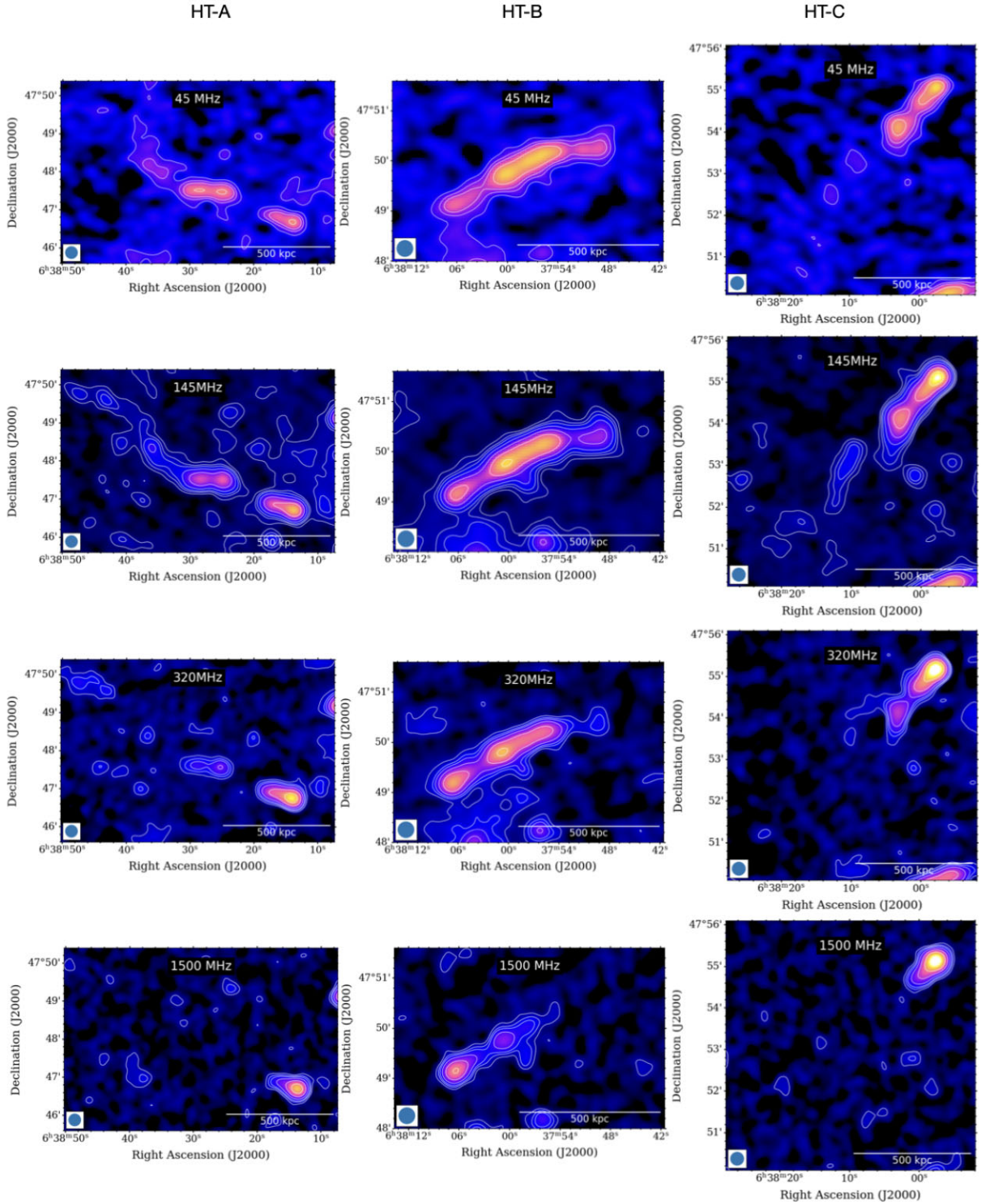
Figure 5. Zoom-in on the source HT-A (first column), HT-B (second column), and HT-C (third column) at all frequencies, from 53 MHz (top) to 1518 MHz (bottom). For each cut-out, the resolution and σ_{rms} are the same as Fig. 4, listed in Table 2.

redshift are present in the DESI DR9 photometric redshift catalogue (Zhou et al. 2021).

In order to identify possible departures from a pure-ageing model (see subsection 3.2 for details), we extracted flux densities and spectral index profiles (Fig. 8). The flux densities are extracted using beam-size sliding regions from the nucleus until the end of the tail, based on their largest linear extent at 144 MHz (Fig. 8, first row). The sliding regions are separated by a few kpc from each other. In this way, we relaxed the requirement of independent measurements, which is not relevant in this case, as we do not use those values for fitting purposes. We then calculated the spectral index profiles between 54 and 144, 144 and 323, and 54 and

Table 2. Images used in this work.

Source	Telescope	Frequency [MHz]	Briggs weighting	Taper FWHM [″]	Resolution [″×″]	$\sigma_{\rm rms}$ [mJy beam^{-1}]	Reference
Halo	LBA	53	−0.25	30	47 × 40	1.80	Fig. 3a
	HBA	144	−0.25	30	41 × 38	0.19	Fig. 3b
	GMRT	323	0	30	40 × 23	0.34	Fig. 3c
	VLA	1518	−0.25	30	37 × 34	0.03	Fig. 3d
HT	LBA	53	−0.25	15	20 × 20	1.22	Fig. 4a
	HBA	144	−0.25	15	20 × 20	0.12	Fig. 4b
	GMRT	323	0	15	20 × 20	0.13	Fig. 4c
	VLA	1518	−0.25	15	20 × 20	0.04	Fig. 4d
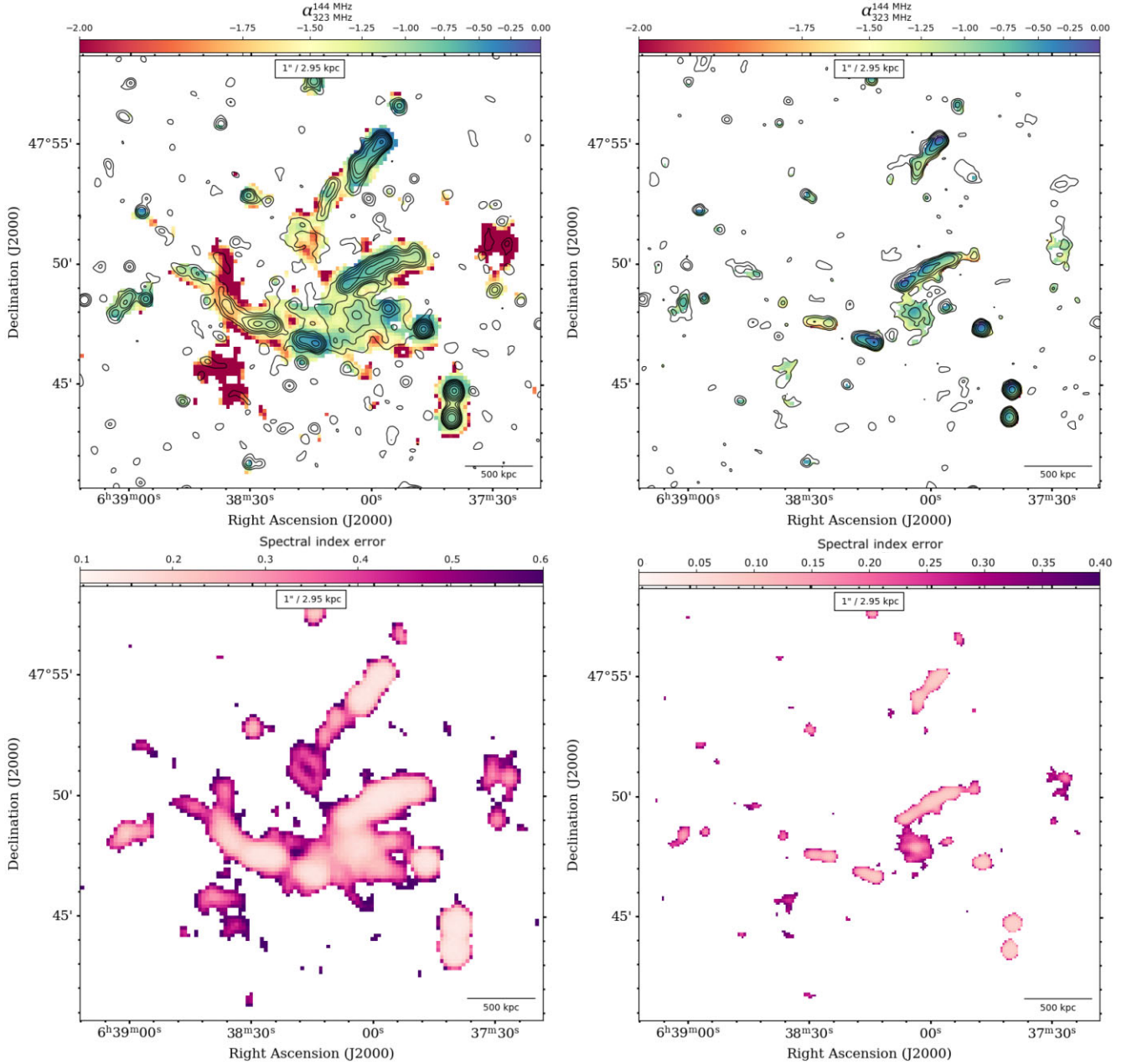
Figure 6. Left panel: Spectral index map between 53 and 144 MHz at a spatial resolution of $36'' \times 36''$ (top) and relative spectral index error $\Delta\alpha^{53\,\rm MHz}_{144\,\rm MHz}$ (bottom). Pixels with surface brightness values below $2\sigma_{\rm rms}$ in the two images were blanked. Black contours start at $3\sigma^{145\,\rm MHz}_{\rm rms}$ and are spaced by a factor of 2. Right panel: Spectral index map between 144 and 320 MHz at a spatial resolution of $20'' \times 20''$ (top) and relative spectral index error $\Delta\alpha^{144\,\rm MHz}_{320\,\rm MHz}$ (bottom). Pixels with surface brightness values below $2\sigma_{\rm rms}$ in the two images were blanked. Black contours start at $3\sigma^{320\,\rm MHz}_{\rm rms}$ and are spaced by a factor of 2.

Table 3. Summary of the properties of the HT galaxies.

Source	RA; Dec.	z_{phot}	d kpc	LLS Mpc	α_{inj}	$v_\perp$ km s^{-1}
HT-A	6: 38: 13.22, +47: 46: 40.44	0.19 ± 0.01	350	1.2	0.43	225
HT-B	6: 38: 06.81, +47: 49: 05.88	0.16 ± 0.01	300	0.6	0.60	274
HT-C	6: 37: 57.52, +47: 55: 09.48	0.18 ± 0.01	870	0.8	0.37	196

Note. Col. 1: Tail name; Col. 2: Coordinate of the optical counterpart; Col. 3: Photometric redshift from (Zhou et al. 2021); Col. 4: Projected distance from the cluster centre; Col. 5: Largest linear extension above $3\sigma_{rms}$ at 144 MHz; Col. 6: injection index $\alpha_{inj} = \alpha_{53\,MHz}^{144\,MHz}$, shown in Fig. 7; Col. 7: tails' projected velocity;
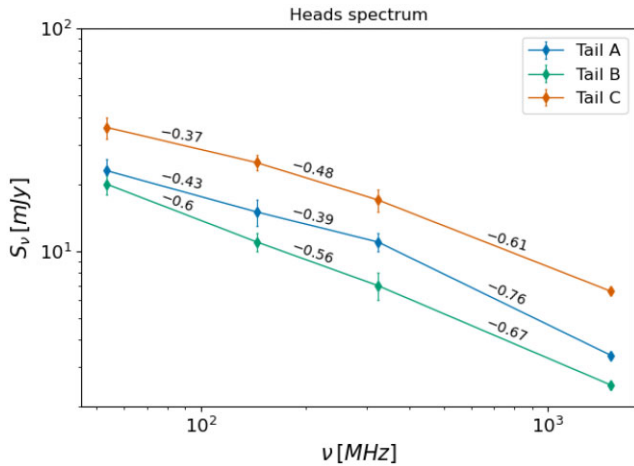
Figure 7. Integrated flux densities of the HTs nuclei, extracted from Fig. 4 in regions with ∼1.5 beam area size.

1518 MHz, considering only the regions with fluxes $\geq 3\sigma_{rms}$ for each pair of frequencies (Fig. 8, second and third row). Another common method to analyse synchrotron spectra is through colour–colour plots (e.g. Katz-Stone, Rudnick & Anderson 1993; Stroe et al. 2013; Edler et al. 2022; Rudnick et al. 2022). This method employs two, two-point power laws to characterize the curved shape of a source spectrum. For these plots, we use measurements made over beam-size separated regions of the source. The results are then compared to the expected trajectories in the colour–colour space, predicted by the standard model of spectral ageing (Fig. 8, fourth row). This method is useful to identify points that still follow the same spectral curvature even though they are spatially distant from each other. In the further section, we describe our model and we study their behaviour separately.

3.2 Spectral ageing

Once injected in the ICM from the AGN, the relativistic plasma starts loosing energy due to synchrotron and IC losses. At the point of the initial acceleration, the energy distribution of the electron population is assumed to be a PL in the form $N(E) = N_0 E^{-\delta}$, where δ is the power-law index. At later times $t > 0$, we expect the energy distribution of the electron population to have a characteristic form depending on t. Since the characteristic time-scale for synchrotron losses is $\propto 1/E$, the electron energy distribution at $t > 0$ will be characterized by a depletion of the highest energy electrons. The same reasoning applies to the synchrotron spectrum, which steepens with time away from the initial PL shape $S \propto \nu^{-\alpha}$ with $\alpha = (\delta - 1)/2$. In the case of HT radio galaxies, this results in a spatial evolution of the spectrum from the head down to the tail. Specifically, the further from the nucleus, the older the electrons, that is, they were accelerated at earlier times, and the more curved the spectrum is expected to be. In the absence of re-acceleration mechanisms, we expect to see the aged synchrotron spectrum assuming a characteristic curved shape.

Here we first consider a pure-ageing scenario to describe the flux and spectral index evolution. One of the most commonly used models to describe ageing of radio galaxies is the Jaffe–Perola (JP; Jaffe & Perola 1973) model. It accounts for ageing of plasma assuming:

(i) negligible adiabatic losses, in line with models where the tail flow is contained and channeled along magnetic field lines;

(ii) a single-initial injection event with given injection index α_{inj}, that represent the plasma spectral index when it is first injected in the ICM by the AGN, that is, before any ageing;

(iii) a given uniform magnetic field that we decide to keep fixed at the minimum ageing value $B = B_{min}$. This choice means maximizing the lifetime of the emitting electrons by minimizing their losses due to synchrotron and IC: higher or lower values of the magnetic field would cause the radio source to fade faster. This equals to $B_{min} = B_{CMB}/\sqrt{3}$, where $B_{CMB} = 3.2 \times (1 + z)^2 \mu$G is the equivalent magnetic field of the Cosmic Microwave Background at the source redshift, which for ZwCl 0634.1+4747 corresponds to $B_{min} = 2.55\,\mu$G.

We calculated the spectra of each head in a region 1.5 times bigger than the beam, centred on the head (Fig. 7). We fix the injection index using the lowest frequencies available in this work $\alpha_{inj} = \alpha_{53\,MHz}^{144\,MHz}$, since they are the less affected by ageing (Table 3).

In order to obtain the JP profiles we used the PYSINCH[2] libraries (presented in Hardcastle, Birkinshaw & Worrall 1998, and subsequent work). Through these libraries, we built an initial electron spectrum (with the injection energy index δ_{inj} derived from the observed $\alpha_{53\,MHz}^{144\,MHz}$) and let it age in the minimum magnetic field condition, following the JP model. We then evolved the JP spectrum at 53, 144, 323, 1518 MHz and obtained the flux density (together with the spectral-index). We normalized the initial JP flux density to the first data point, which corresponds to the head of the tail. The time-ageing of the JP model spectra can be converted to space-ageing along the tail, considering a given constant velocity. We thus obtain a rough estimation of the projected velocity on the plane of the sky $v_\perp$ which is of the order of $200 - 300$ km s^{-1} (Table 3). We point out that this is a lower limit for multiple reasons. First, magnetic field and velocity are strongly correlated, which means that it is not possible to discern between the minimum ageing scenario and any other value of the magnetic field B, far from B_{min}, combined with higher velocities of the tail. Secondly, this velocity is projected, meaning that there could be a non-negligible component along the line of sight.
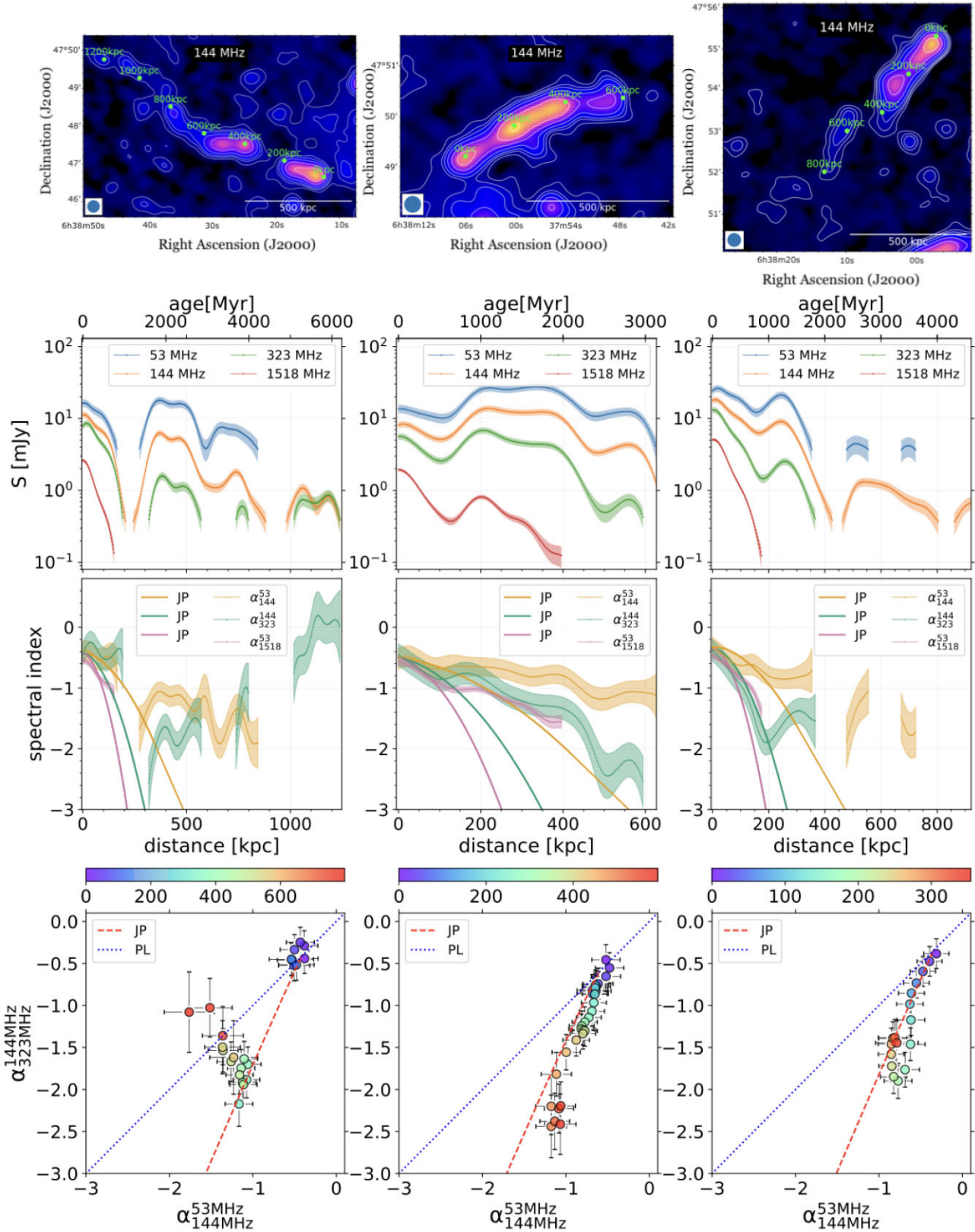
[2]https://github.com/mhardcastle/pysynch

Figure 8. First row: HT extension at 144 MHz, where the tails are more visible. Reference points are shown to help the reader in matching the profiles with images; Second row: flux profile; Third row: spectral index profile considering regions with flux above $3\sigma_{rms}$; Fourth row: three frequency (53, 144, 323 MHz) colour–colour plot with the bisector indicating the set of point where $\alpha^{53}_{144} = \alpha^{144}_{323}$, which means that the spectrum resembles a power law (PL). The dashed red line represents the curved spectrum ($\alpha^{53}_{144} > \alpha^{144}_{323}$) of the JP model. The colourbar reflects the distance from the head of each point. The profiles are shown for HT-A (first column), HT-B (second column), and HT-C (third column).

The geometry of this scenario includes the tail travelling outward from the cluster centre with an angle $\theta_0 = 60°$ to the line of sight. This model was able to explain the high-frequency radio observations for reasonable choices of the model parameters, as for example the velocity of the tail of the order of $\sigma_v \sim 1400\,\mathrm{km\,s^{-1}}$. Nonetheless, they did not detect any shock at the jump position in the X-ray image. Thus they concluded that, if the shock is present, it should be moving with a significant inclination with respect to the plane of the sky (see fig. 13 in Cuciti et al. 2018).

Our results at high frequencies are consistent with the brightening starting at ~ 150 kpc, and the subsequent spectral flattening. As a reference with the analysis of Cuciti et al. (2018), in Fig. 9 we show α_{53}^{144} compared to α_{323}^{1518}. The spectral profile shows a peculiar feature: the flattening starts at different distances depending of the frequencies used. To better appreciate this feature, we zoom in the first 400 kpc of HT-B and performed spectral index profiles comparing α_{144}^{53}, α_{323}^{144} and α_{1518}^{323}. In Fig. 9, the flattening point appears to be spatially shifted from 150 (α_{1518}^{323}) to 110 (α_{323}^{144}) and 80 kpc (α_{144}^{53}). This frequency-dependent feature would discourage the shock scenario, since the latter would create re-energization feature happening simultaneously at the same point of the tail. We discuss and test possible scenarios in Section 4. Interestingly, we also find a residual emission with $\alpha_{144}^{53} < -2.5$ at the very end of the HT B (Fig. 4). This is clearly visible only in the LOFAR low-frequencies images and after a region where there is no emission. If this steep spot is part of the tail, the total extent of the HT galaxy would be of 1.2 Mpc. However, we cannot rule out that it may be a residual emission, also present in other parts of the image. In addition, given the large distance and the significant spectral index uncertainty associated with it, we exclude the radio spot from further analysis.

HT-B is the tail with the most extended frequency coverage. This means we can follow the flux density and spectral index evolution up to ~ 400 kpc at all the available frequencies in this work. Therefore, in addition to the profiles shown in subsection 3.2, we performed local spectral fitting along HT-B. This allows us to study possible variations of the synchrotron spectrum along the tail. To do that, we extracted the spectra in eight circular beam-size independent regions along the source and fitted each local spectrum with a JP model using SYNCHROFIT[3] package. The result of the local JP fitting is shown in Fig. 10. The model has three free parameters: the energy injection index δ_{inj}, the break frequency ν_{break} and the normalization factor N for correct scaling. From the synchrotron theory (see e.g. Longair 2011), the break frequency is related to the spectral age t_s as

$$t_s = 1.61 \times 10^3 \frac{B^{0.5}}{(B^2 + B_{\mathrm{CMB}}^2)(\nu_{\mathrm{break}}(1+z))^{0.5}} \quad \mathrm{Myr}, \qquad (2)$$

where the magnetic field B and the equivalent magnetic field of the CMB B_{CMB} are in μG, while ν_{break} in GHz. The initial energy spectrum spectrum undergoes a gradual transformation, with an exponential decline emerging beyond the point ν_{break}. If no source of re-acceleration is present, the measured break frequency decreases systematically along the tail as $\nu_{\mathrm{break}} \propto t_s^{-2}$. In the approximation of constant velocity that leads to $\nu_{\mathrm{break}} \propto d^{-2}$, in agreement with the scenario in which the oldest particles are those at a larger distance from the AGN. We first fitted the spectra with the injection index free to vary in the range [1.5, 3.5] (purple, Fig. 11). We noticed that the injection index does not show a clear trend but fluctuates around 2.2 ± 0.2. Thus we fitted again the same regions fixing the energy injection index to 2.2 (i.e. $\alpha_{\mathrm{inj}}{=}0.6$), which is also in

Figure 9. Spectral index profile for HT-B: comparison between α_{144}^{53}, α_{323}^{144} and α_{1518}^{323}. Vertical lines trace the shift of the flattening point from ~ 150 to ~ 110 and ~ 80 kpc.

3.2.1 HT A

The radio galaxy HT A shows unusual properties: after the bright nucleus (the head), we note another bright peak in the surface brightness at ~ 380 kpc (Fig. 8, second rows). Correspondingly, the spectral index profile shows a flattening, jumping from ~ -0.5 of the head to ~ -1.5 and then stabilizing at ~ -1.3 in both α_{53}^{144} and α_{144}^{320}. The flattening extends to ~ 550 kpc (Fig. 8, third rows). We overplot the JP model (solid lines) for all frequencies. Up to 200 kpc, the spectral index profile decline as expected due to radiative losses of the electron population accelerated by the radio galaxy. In this first part, the JP model is able to reproduce the profiles. At larger distances, it is not trivial to account for the bump in the flux density profile and the flattening of the spectral index, using this pure-ageing scenario. Moreover, the colour–colour plot shows that points corresponding to 380–550 kpc are progressively moving from the expected curved JP towards the power-law line. That means the shape of the spectrum is getting flatter instead of continuing the steepening due to ageing. Thus, we conclude a mechanism able to re-energize the relativistic population of CRe, initially injected by the AGN, must have occurred. We also note that there are few points in the range 740–800 kpc from the head that surprisingly cross the power-law line, lying in the area where $\alpha_{144}^{323} > \alpha_{53}^{144}$. We argue this is an effect due to mixing of the electrons along the line of sight. Such an effect is common at very large distances from the AGN.

3.2.2 HT B

Using GMRT and VLA observations, Cuciti et al. (2018) found a surface brightness jump at ~ 150 kpc from the head of the tail, in correspondence with a flattening (150–300 kpc) of the spectral index. This was interpreted as evidence for electron re-energization and they suggested that an interaction with a shock can explain the brightness and spectral index properties. The proposed scenario included the presence of a weak shock (Mach number $\mathcal{M} \lesssim 2$), moving from the back end of the tail until the point of the brightness bump ~ 200 kpc.

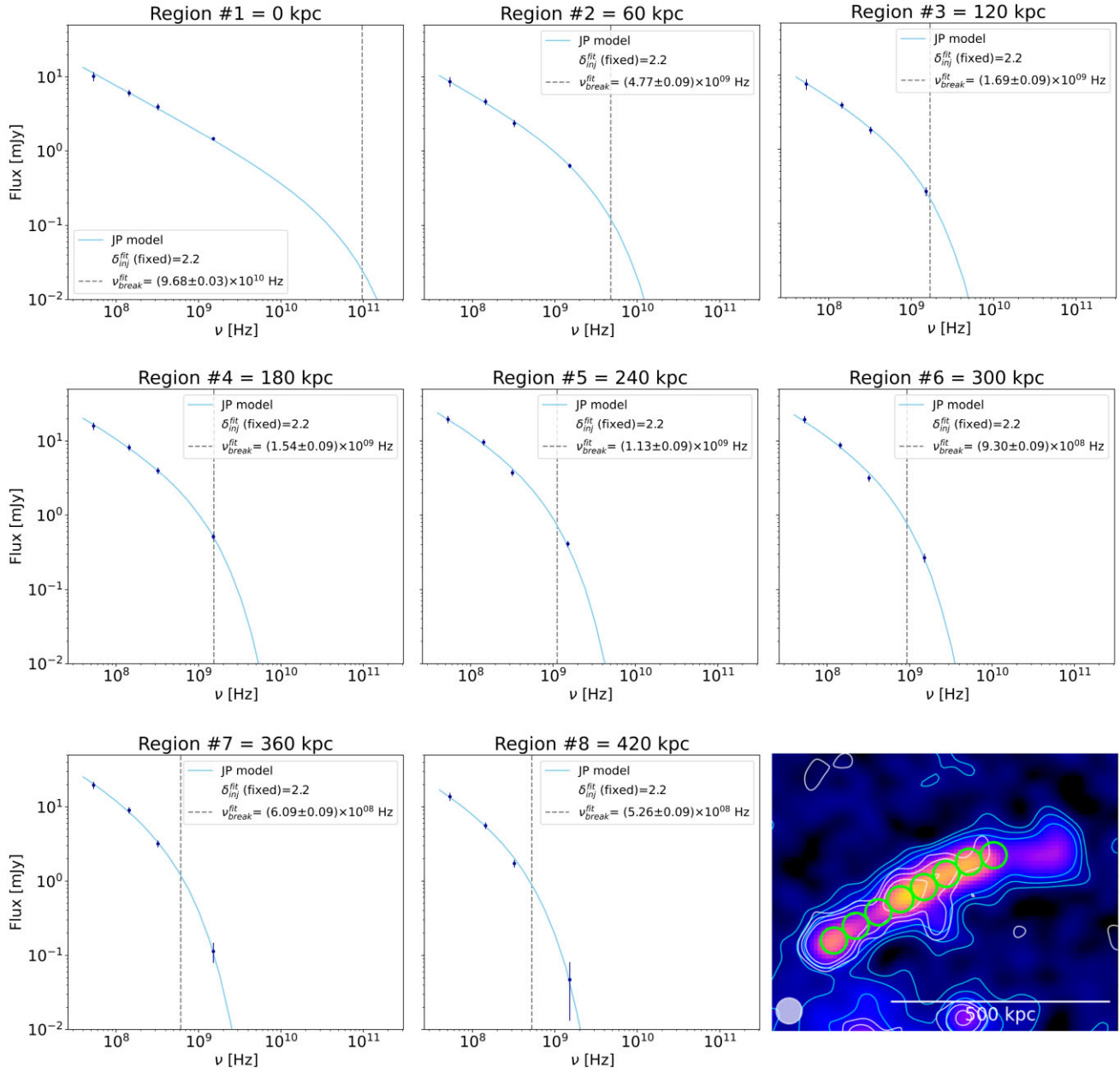[3]https://github.com/synchrofit/synchrofit

Figure 10. Spectra extracted in 8 circular beam-sized independent regions along the HT-B. The light blue line represent the best fit of the JP model and the model parameters (δ_{inj}, ν_{break}) are listed in the legend of each plot. The image of HT-B at 144 MHz is shown in the bottom right panel with the 8 regions overlapped. We plot the 3-, 6-, and $12\sigma_{rms}$ contours at 144 (cyan) and 1518 (white) MHz, as a reference of the tail extension at different frequencies.

agreement with the low-frequency power-law index of synchrotron emission, $\alpha_{53\,MHz}^{144\,MHz}$, observed of HT-B (Fig. 7). Thus we can limit the number of free parameters and we show the trend of the best fit parameters ν_{break} and δ_{inj} in Fig. 11 (teal). Keeping δ_{inj} fixed or free to vary, does not influence the overall trend of the frequency break along the tail. Interestingly, we notice that after an initial decrease (up to region 3), the break frequency remains fairly constant. The distance at which this happens coincides with the distance of the spectral index flattening at ~150 kpc. This confirms that at some point along the tail, there must be a mechanism that stops the natural ageing (spectral index flattens and the break frequency stops decreasing). To quantitatively assess the slowdown of the break frequency steepening, we employed a general power-law model of

the form $f(d) \propto d^{-a}$ to fit the data points spanning from Region 2 to 8 (Fig. 11, left), where d is the distance from the core and a the power-law index. We excluded the break frequency value in Region 1, as is strongly vary among the two JP fitting models, and it can be considered as a lower limit since it is much higher than the highest spectral point in the case $\delta_{inj} = 2.2$. The best fit (blue solid) shows a power-law index $a = 1.06 \pm 0.09$. Notably, this value indicates a slower rate of change compared to expected law based on the relationship between spectral age and break frequency (see equation 2) and assuming a constant tail speed, $\nu_{break} \propto d^{-2}$ (dashed-blue line for comparison). Similar evidence has been found in (Parma et al. 1999), who claimed re-acceleration processes for four of the radio galaxies in their sample.
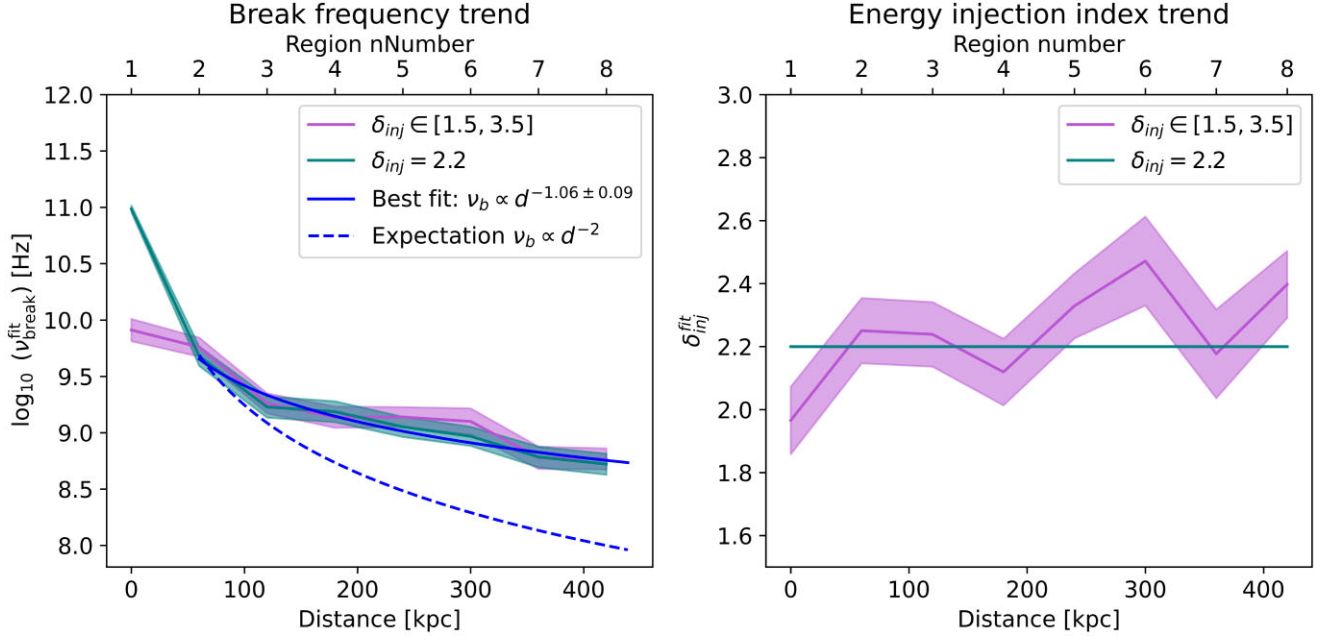
Figure 11. Best fit break frequency and energy spectral index trend along HT-B. In purple the result with energy injection index free to vary, $\delta_{inj} \in [1.5, 3.5]$; in teal it is kept fixed $\delta_{inj} = 2.2$ (i.e. $\alpha_{inj} = 0.6$, in agreement with the HT-B head spectrum of Fig. 7). Left panel: A power-law function was fitted to ν_{break}^{fit} corresponding to regions number 2–8. The best fit power-law index results to be $a = -1.06 \pm 0.09$ (blue solid line). The break frequency trend expectation from a pure ageing scenario $\nu_{break} \propto d^{-2}$ is plotted as a reference (blue dashed line).
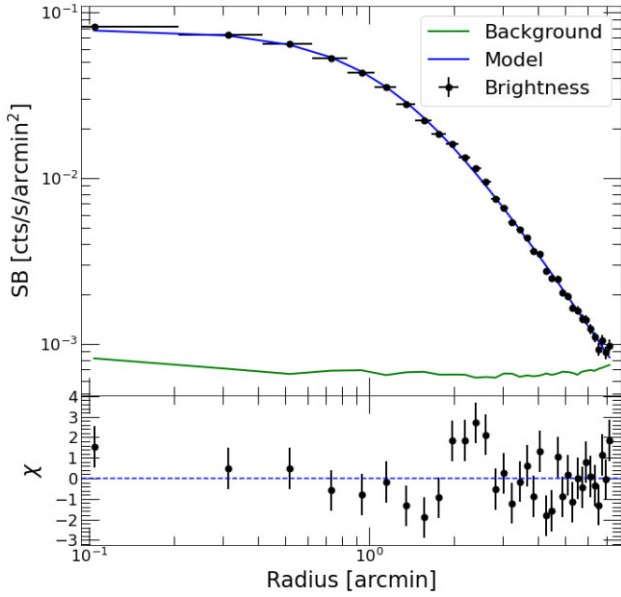
Figure 12. Surface brightness profile with the fitted single β-model. The best fit parameters are $\beta = 0.59 \pm 0.05$, $r_c = 1.24 \pm 0.02$ arcmin, $I_0 = 0.079 \pm 0.006$ cts/s/arcmin^2, with a reduced $\chi^2 = 1.2$.

Figure 13. X-ray 0.5–2 keV image filtered with an adaptive GGM filter, using a signal-to-noise ratio of 32. Radio contours from Fig. 4b are overplotted.

3.2.3 HT C

Analysing HT C is difficult because of its morphology and extension. In fact, the radio galaxy is more compact at $\sim$GHz frequency (see also Fig. 5), while revealing a longer structure only in LOFAR images. Nevertheless, also in this case a pure-ageing JP model cannot account for the emission observed at distances larger than 200 kpc. Again, we see evidence for re-energized CRe left behind the AGN. These CRe do not age as expected by the considered model: the flattening
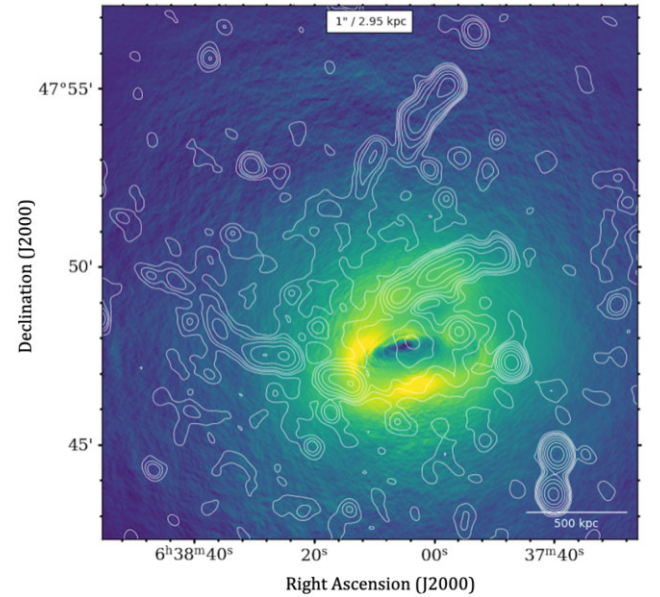
of the spectral index implies that the energy distribution of the CRe is boosted toward higher energies.

3.2.4 Other ageing models

Another widely used model for spectral ageing is the Kardashev (1962) and Pacholczyk (1970) model (KP). The JP and KP models differ in the treatment of the emitting electrons' pitch angles, that

is, the angle between the magnetic field **B** and velocity **v** of the charged particle. In the KP model, the pitch angles of the electrons are fixed over their radiative lifetime, while in the JP model, pitch angle scattering takes place. This difference influences the way CRe lose energy, and thus, affects the resulting synchrotron spectra (Harwood et al. 2013). The pitch angle scattering of the JP model is a more likely scenario than that of the fixed pitch angles of the KP model (Tribble 1993). The reason for this is that for a turbulent magnetic field configuration, the expected resonant scattering of the particles is effective on scales comparable to the Larmor radius of CRe, and thus smaller than the resolution of observations (Carilli et al. 1991; Hardcastle 2013). Finding the best model for radiative ageing is beyond the scope of this work (see Section 4). We note that the differences between JP and KP model spectra would not change our conclusion, that is, standard ageing cannot account for the observed profile and thus other re-acceleration mechanisms need to operate in this system.

3.3 X-ray properties

We use *XMM–Newton* observations to study the environment of the HT galaxies, that is, the ICM that deflects their jets. From previous studies, it is known that this cluster appears to be in a non-relaxed state (Cuciti et al. 2015).

3.3.1 Surface brightness profile

We first studied the X-ray surface brightness to check for jumps in the azimuthal profile. We used `pyproffit`[4] (Eckert et al. 2020) to compute and model the surface brightness with a single, spherically symmetric β-model (Cavaliere & Fusco-Femiano 1976) of the form:

$$I(r) = I_0 \left[1 + \left(\frac{r}{r_c} \right)^2 \right]^{-3\beta + 0.5} + b, \tag{3}$$

where I_0 is the central surface brightness, r_c the core radius, β describes the ratio between thermal and gravitational energy of the plasma, and one additional parameter b to describe the background (Eckert et al. 2020). We extracted a profile in circular annuli centred on the X-ray peak, with a bin size of $15''$ until R_{500}. The azimuthal fit shows that a smooth β-model accounts for the emission, which does not show bumps or discontinuities (Fig. 12).

3.3.2 Gaussian gradient magnitude filter

In order to look for features in the ICM that can be connected to the HT galaxies, we used standard X-ray image processing techniques. When studying galaxy clusters, particularly relaxed objects, the bright core of ICM emission gives rise to steeply peaked surface brightness profiles, where it can be difficult to detect variations such as edges, filaments, cavities, or ripples. Thus, filtering techniques are frequently used to see and enhance variations in the surface brightness distribution. Among the different techniques, we used the adaptive version of the Gaussian Gradient Magnitude[5] (GGM; Sanders et al. 2016a, b) filter. In standard GGM filter, the image is convolved with a function that is the gradient of a Gaussian with a particular scale, measuring the gradients on this scale. This is a useful method to detect edge-like structures, such as shocks and cold fronts, which lead to strong gradients (Sanders et al. 2018). Since

the accuracy of the gradient depends on the number of counts within the scale probed, this standard GGM filtering becomes noisier in regions where the count rate is lower, that is, the outskirts of galaxy clusters. Therefore, we used the adaptively smoothed GGM described in Sanders et al. (2022) that dynamically choses the appropriate scale that reduces this effect. The main input parameter of this software is the signal-to-noise ratio, which is used to calculate the smoothing scale from the input counts. Following Sanders et al. (2022) we set it to 32, and we used the image counts in the energy band from 0.5 to 2 keV. We note the presence of bright regions, that is, high gradient values, in the central left part of the GGM-filtered image (Fig. 13) but this region does not intersect any of the tails. Hence, we conclude that the ICM does not show features that appear to interact with the radio tails.

3.4 Radio halo morphology

Based on the $3\sigma_{\rm rms}$-contours, the radio halo in ZwCl 0634.1+4747 has a diameter of $\sim$400–800 kpc in the E–W direction, depending on the frequency (see Table 4).

Following the procedure of Cuciti et al. (2018), we measure the flux density within a circular area of $\sim$600 kpc diameter, which roughly follows the $3\sigma_{\rm rms}$-contours of the images (see Fig. 3), using the source-subtracted tapered images described in subsection 2.5. This region avoids the two HT-A and HT-B radio galaxies, which are extended sources, and thus cannot be subtracted from the *uv*-data with the same procedure used for the compact sources in subsection 2.5. The results are listed in Table 4. We point out that we find high-frequency flux densities that are slightly different from Cuciti et al. (2018). Our values of $S_{1.5\,{\rm GHz}} = 2.5 \pm 0.2$ mJy and $S_{320\,{\rm MHz}} = 14 \pm 2$ mJy are nevertheless still consistent with measurements reported in Cuciti et al. (2018). The difference could be due to different sources subtraction methods. Cuciti et al. (2018) measured the compact-sources flux density from the high-resolution images and subtracted that from the measurement on the radio halo region of the low-resolution images, while here we subtracted the compact sources directly from the *uv*-data.

In order to obtain a size and flux estimate that is independent of the signal-to-noise ratio of the radio images (i.e. that does not rely on the $3\sigma_{\rm rms}$ − contours), we fit the the same low-resolution source-subtracted images of Fig. 3 with Flux Density CAlculator software[6] (`FDCA-Halo`; Boxelaar, van Weeren & Botteon 2021). This method fits the surface brightness profile of haloes to a 2D-model using Bayesian inference. The general exponential model used is

$$I(\mathbf{r}) = I_0 e^{-G(\mathbf{r})}, \tag{4}$$

where $I(\mathbf{r})$ is the surface brightness and $G(\mathbf{r})$ the function that takes different forms depending on the complexity of the model (see Boxelaar, van Weeren & Botteon 2021, for details). In the circular model case, $G(\mathbf{r}) = |\mathbf{r}|/r_e$, where the e-folding radius r_e is the length-scale at which the surface brightness drops to I_0/e. To avoid contaminating sources, we first masked the regions corresponding to extended radio sources other than the radio halo. Masked regions, model and residuals can be found in Appendix A, while the fitting results in Table 4.

The fitted r_e values are more uniform across the frequency range (120 − 145 kpc) compared to the size based on the $3\sigma_{\rm rms}$-contours ($D \sim 480 − 850$ kpc) and consistent with each other because they are less affected by the noise. Flux densities with `FDCA-Halo` are

---

[4] https://github.com/domeckert/pyproffit
[5] https://github.com/jeremysanders/ggm

[6] https://github.com/JortBox/Halo-FDCA

Table 4. Summary of the main radio halo properties.

ν MHz	D kpc	$S_\nu(< 300\,\text{kpc})$ mJy	P_ν W Hz^{-1}	I_0 μJy/arcsec^2	r_e kpc	$S_\nu^{\text{FDCA}}(< 3r_e)$ mJy	P_ν^{FDCA} W Hz^{-1}
53	770	138 ± 16	$(1.2 \pm 1) \times 10^{25}$	16 ± 2	141 ± 14	184 ± 27	$(1.6 \pm 0.2) \times 10^{25}$
144	850	40 ± 4	$(3.5 \pm 0.3) \times 10^{24}$	4.5 ± 0.3	145 ± 7	54 ± 6	$(4.7 \pm 0.2) \times 10^{24}$
320	480	14 ± 2	$(1.2 \pm 0.2) \times 10^{24}$	2.1 ± 0.5	130 ± 28	20 ± 6	$(1.8 \pm 0.5) \times 10^{24}$
1518	530	2.5 ± 0.2	$(2.2 \pm 0.2) \times 10^{23}$	0.36 ± 0.04	120 ± 12	3.0 ± 0.3	$(2.6 \pm 0.3) \times 10^{23}$

Note. Col. 1. Frequency; Col. 2. Linear extension corresponding to the $3\sigma_{\text{rms}}$ contour in the E-W direction as a size reference; Col. 3. Flux density measured within a circular region with $R = 300\,\text{kpc}$ (see Fig. 3); Col. 4. Radio power calculated from $S_\nu(< 300\,\text{kpc})$ with the K-correction applied, assuming $\alpha = -1.2$; Col. 5. Central surface brightness from FDCA-Halo fitting, using a circular halo model; Col. 6. e-folding radius from FDCA-Halo fitting, using a circular halo model; Col. 7. Flux density measured within the $3r_e$ calculated by FDCA-Halo; Col. 8. Radio power calculated by FDCA-Halo corresponding to $P_\nu^{\text{FDCA}}(< 3r_e)$, assuming $\alpha = -1.2$
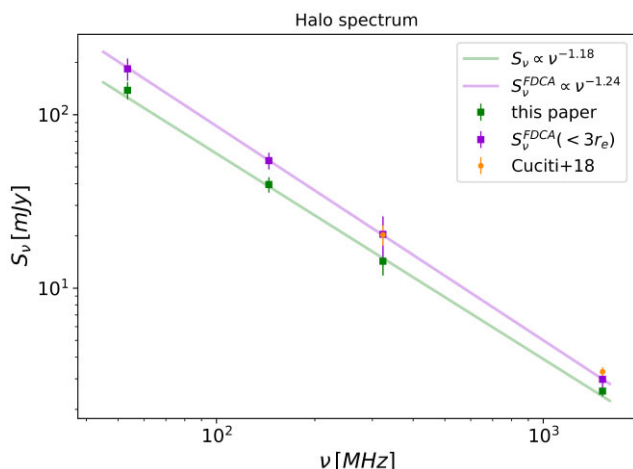
Figure 14. Integrated spectrum of the radio halo from 1.5 GHz down to 53 MHz. Green points indicate the integrated flux values measured in a circular region with $R = 300\,\text{kpc}$. Purple points represent $S_\nu^{\text{FDCA}}(< 3r_e)$, the flux calculated via FDCA-Halo fitting procedure within three e-folding radii. Values at 320 MHz and 1.5 GHz from Cuciti et al. (2018) are displayed in blue.

integrated up to a radius $R = 3r_e$ that contains 80 per cent of the total flux $S_\nu(< 3r_e) = 0.8 S_\nu^\infty$ (Murgia et al. (2009)).

To date, this is one of the few radio haloes where we can study the radio spectrum from 1.5 GHz down to 50 MHz. In the near future, observations by the LOFAR LBA Sky Survey (LoLSS; de Gasperin et al. 2021, 2023), combined with archival data from other telescopes (such as uGMRT and VLA), will increase the number of systems with such a large frequency coverage (Pasini et al., in prep.).

The spectrum of the radio halo in ZwCl 0634.1+4747 is shown in Fig. 14: green points represent flux densities extracted within a radius of 300 kpc $S_\nu(< 300\,\text{kpc})$, while purple points are values obtained via FDCA-Halo procedure $S_\nu^{\text{FDCA}}(< 3r_e)$. We note that the fitted size of the halo, that is, $3r_e$, is wider than the circular extraction region with $R = 300\,\text{kpc}$ (based on the $3\sigma_{\text{rms}}$ − contours), and thus the FDCA-Halo flux is higher. Despite of this, the spectral shape remains unchanged (Fig. 14). We fit the spectrum using a PL, finding a best fit spectral index between 53 and 1518 Hz of $\alpha = -1.18 \pm 0.04$ and $\alpha^{\text{FDCA}} = -1.24 \pm 0.03$, respectively. These values are consistent with previous high-frequency (Cuciti et al. 2018) and low-frequency (Cuciti et al. 2022) studies. Spectral indices $\alpha < -1.1$ are expected for the radio haloes and are in agreement with other radio haloes studied over the whole radio spectrum (e.g. A1758 Botteon et al. (2018, 2020), Coma Bonafede et al. (2022)). Moreover, this halo is underluminous in the power-mass correlation in both $P_{1.5\text{GHz}} - M_{500}$ (Cuciti et al. 2021) and $P_{150\text{MHz}} - M_{500}$ (Cuciti et al., submitted); and has an emissivity $J_{1.4\text{GHz}} = (3.2 \pm 0.2) \times 10^{-43}$ erg (s cm^{3}Hz)$^{-1}$

slightly lower compared to the emissivity of classical radio haloes at 1.4 GHz in the range of $[5 \times 10^{-43}; 4 \times 10^{-42}]$ erg (s cm^{3}Hz)$^{-1}$ (Cuciti et al. 2022). Statistical studies showed that haloes not lying on the $P_{1.5\text{GHz}} - M_{500}$ correlation are usually associated with non-merging clusters or with USSRHs. In the framework of the turbulent re-acceleration scenario, this means that either the radio halo is not present at all, or the system is less massive and has experienced minor mergers, thus producing radio haloes with steeper spectra.

4 DISCUSSION

In this work, we studied HT radio galaxies that show ripples in the surface brightness profiles and spectral index flattening along the tail. In order to assess whether this is in line with pure radiative ageing due to IC and synchrotron losses, we compared the data to the JP model. This is a standard and widely used spectral ageing model, that assumes electrons are injected with a constant power-law energy spectrum. Moreover, in this analysis, we work under the assumptions of uniform minimum magnetic field, constant velocity and fixed inclination of the radio galaxy (see subsection 3.2). Though simple, these are reasonable hypotheses given, for example, that the tails do not show sudden changes in direction. More complex models that include variations of the magnetic field etc. would require more data. Our results show that the jet emission deviates from the pure radiative ageing due to IC and synchrotron losses. We conclude that this is evidence for re-acceleration. In this section, we discuss possible scenarios that can affect the tail's spectral behaviour and morphology. Particular focus is on the long flattening of the spectral index and a frequency-dependent feature, only clearly visible in HT B (Fig. 9). This is due to the lack of high frequency information to use for measuring the spectral index α_{323}^{1518} at distances >150–200 kpc from the head for HT A and HT C.

A first simple explanation for ripples in the brightness profile can be a varying output of the AGN. The standard JP model (subsection 3.2) uses a single injection event. Thus, we are assuming that the AGN injection rate remains constant with time. A varying AGN would reproduce the ripples in the surface brightness profiles but not the flattening in the spectral index that we see in Fig. 8. Thus, although a varying AGN is still a plausible mechanism that contributes to the observed profiles, we exclude it as the main mechanism creating the observed features. We point out that possible changes of inclination during the motion through the cluster can also alter the observed surface brightness and spectral index profiles, causing deviations from the expected JP profile. However, we argue that this scenario is very unlikely for two main reasons. First, the morphology of the tails does not show sharp bends that could suggest such a scenario of varying direction of motion. Secondly, even if projection effects happened along the tail, in those regions we would be summing younger 'foreground' electrons with older 'background'

ones. The result would be a spectral index decreasing faster with respect to the standard ageing, not slower, as we observe.

4.1 Shock–tail interaction

The interaction between shocks and tails is a possible scenario that can alter the tail morphology and physical properties. It is well known that when a shock encounters a population of aged electrons, it can re-energize particles, leading to observable synchrotron emission. However, the expected very high sound speed of the relativistic plasma does not allow the shock to penetrate into the radio tail (Enßlin & Gopal-Krishna 2001).

However, a shock can adiabatically compress the fossil plasma and increase the magnetic field (Enßlin & Gopal-Krishna 2001; Enßlin & Brüggen 2002). In fact, adiabatic compression is able to re-energize an electron population, inducing brightening, and spectral flattening. This kind of interaction was already investigated in the past, either in combination with the presence of a shock (van Weeren et al. 2017; Botteon et al. 2019; Wilber et al. 2019), or a cold front (Botteon et al. 2021; Giacintucci et al. 2022). The shock scenario was also proposed by Cuciti et al. (2018) as a possible explanation to the HT-B observed radio properties. There are very few examples of HT-radio galaxies formation (O'Neill et al. 2019a) or shock-radio galaxy interaction (Nolting et al. 2019a, b; O'Neill et al. 2019b) simulations in the literature that can shed light on this complicated scenario. Although none of these simulations are tuned to reproduce the geometrical configuration proposed by Cuciti et al. (2018), we can use them for a general comparison. In particular, Nolting et al. (2019a) studied the interaction between a shock and an active radio galaxy, in the case where jets are aligned with the shock normal. They show that, as the shock travels along the jets, vortices are generated behind it (see Fig. 5 of Nolting et al. (2019a)). This toroidal vortex was found also in other simulations of a shock wave interacting and adiabatically compressing a radio plasma cocoon (Enßlin & Brüggen 2002; Pfrommer & Jones 2011). The fact that we do not observe this morphological feature suggests that there is no shock travelling through the tail. However, we cannot completely rule out this option since signs of jets disruption might be present on scales smaller than our resolution. Moreover, we point out the need of tailored simulations, where a shock crosses a HT radio galaxy whose morphology has been already modified by the interaction with the ICM. As mentioned in subsection 3.2, a shock interacting with the tail in the same configuration proposed by Cuciti et al. (2018) would create re-acceleration features at the same point of the tail (i.e. simultaneous brightness jumps and flattening of the spectra in correspondence of the shock location), while in HT-B we observe a shift of the point where the spectrum flattens (Fig. 9). This will be discussed in detail in subsection 4.2. Finally, we point out that the *XMM–Newton* observation does not show any shocks at or near the radio tails, (see subsection 3.3). For all the arguments mentioned above, we consider the presence of a shock as an unlikely scenario to explain the data.

4.2 Turbulence

Turbulence within the tail can arise from hydrodynamic instabilities that result from the interaction between the relativistic plasma and the surrounding medium. (Mignone, Massaglia & Bodo 2004; Jones et al. 2017; Kundu, Vaidya & Mignone 2021; Mukherjee et al. 2021; Ohmura et al. 2023). This turbulence can trigger several mechanisms of stochastic acceleration of particles, such as gentle acceleration,

which has been suggested as a possible explanation for the GReET in Abell 1033 (de Gasperin 2017; Edler et al. 2022).

As mentioned in subsection 3.2, data for HT-B suggest that the spectral index flattens at different distances, depending on the frequency. In particular, the spectrum measured at higher frequencies flattens at greater distances from the head. Considering the kinematics of the tails, this corresponds to a situation in which the spectrum at higher frequencies flattens over longer times. This scenario agrees with the fact that spectral flattening is more evident at higher frequencies: α_{53}^{144} remains almost constant in the first 400 kpc around a value of -0.6, -0.8, while α_{323}^{1518} shows a well-defined decrease up to ~ -1.4 before flattening (see Fig. 9). This evidence allows us to understand something more about the mechanisms of particle re-acceleration. In practical terms, the flattening of the spectrum at higher frequencies over longer times indicates a gradual shift of the particles towards high energies. This, in turn, places constraints on the re-acceleration times. Fig. 9 suggests that the energy of the emitting electrons essentially doubles in about 80 kpc, corresponding to about 260 Myr (considering a speed of the tail ~ 300 km/s). We can conceive of two scenarios. In the first scenario, the electrons cool due to losses for a time t_{start} without being re-accelerated. After a time t_{start}, necessary for the development of the instabilities in the head tail and possibly also necessary for the turbulence to cascade to resonant scales, the same particles are re-accelerated on a time-scale, τ_{acc}. This causes the spectrum to increase again at higher energies if $\tau_{acc} < t_{start}$ ($\tau_{acc} \geq t_{start}$ would otherwise simply balance cooling on time-scales τ_{acc}). In this case, $\tau_{acc} \sim 260$ Myr and $t_{start} \sim 500$ Myr (from kinematics $\sim$ distance spectral flattening/velocity). A second option could be that a second component of (relativistic) particles is re-accelerated starting at t_{start} with $\tau_{acc} \sim 200$–300 Myr. These particles might be present in the tail at lower energies and potentially filling a different volume with respect to the other component. This second scenario could explain the strong brightness increase observed in the re-acceleration phase and might also suggest that volume is not uniformly filled with CR particles. Discriminating between the two possibilities and constraining model parameters by fitting the data is beyond the scope of the current work and will deserve a future study. Finally, we point out that galaxies in clusters are expected to move with a velocity of the order of the velocity dispersion ($\sim 10^3$ km s^{-1}), which is not compatible with the value of a few hundreds km s^{-1}, derived from our modelling in subsection 3.2. This suggests deficits in the JP model, even in the first kpc from the AGN. This means that no part of the tail is ageing subject to pure radiative synchrotron and IC losses, and we are facing a mechanism that acts broadly along the tail and starts as soon as the jets interact with the external medium. Recent simulations by Ohmura et al. (2023) show the effect of turbulent re-acceleration on HT galaxies. They simulated AGN jets in an ICM wind and computed the evolution of CRe, considering both energy losses and stochastic acceleration. Their work clearly shows that in the presence of re-acceleration, the spectral index does not decrease substantially along the tail but remains fairly flat ($\alpha_{600}^{150} \sim -0.8$, -1) for about 150 Myrs. This is in agreement with our observations at low frequencies. At higher frequencies, we find a decrease of the spectral index in the first kpc from the head, which we attribute to the factors described earlier.

5 CONCLUSIONS

In this work, we have studied the radio halo and three HT radio galaxies of the same cluster ZwCl 0634.1+4747($z = 0.174$). We make use of LOFAR LBA 53 MHz, LOFAR HBA 144 MHz, GMRT 323 MHz, VLA 1.5 GHz, and X-ray *XMM–Newton* data. The cluster

has already been studied at higher frequencies (Cuciti et al. 2018). However, the addition of low-frequency LOFAR observations has enabled us to study low-brightness emission on large scales, both, in terms of diffuse halo emission and radio galaxies.

Our main results can be summarized as follows:

(i) We studied three HT radio galaxies, spread over the whole cluster volume. Their properties are listed in Table 3. This is the first time where multiple tails belonging to the same cluster can be studied over a frequency range from 53 to 1518 MHz. The use of very low-frequency observations allowed us to observe them up to ∼1 Mpc projected size and study the spectra at very large distances from the head.

(ii) We investigated the properties of the HT galaxies by extracting surface brightness and spectral index profiles, revealing an increase of surface brightness and flattening of the spectral index. These characteristics together with their considerable lengths point towards a process that involves the re-acceleration of the initial electron population, which otherwise would cool below energies capable of radiating at our reference radio frequencies.

(iii) We have proposed a scenario that could explain the morphological and spectral properties of the HT galaxies. This scenario involves a turbulence-induced, gentle re-acceleration mechanism that could explain the long flattening of the spectral profiles and the frequency-dependent feature of Fig. 9. We propose two scenarios: one involving a standard single population of electrons which initially cools down and then starts to be re-accelerated after t_{start}; a second one, including multiple components of relativistic particles that are activated at different times. Regardless of the scenario, the re-acceleration mechanism would act on a characteristic time-scale τ_{acc} ∼200–300 Myr or shorter, derived by comparing the distances at which the spectrum at different frequencies flattens.

(iv) ZwCl 0634.1+4747also hosts a radio halo with a linear size varying from ∼400 to 800 kpc, depending on the frequency. We find that the spectrum is well represented by a PL with a spectral index between 53 and 1518 MHz of $\alpha^{FDCA} = -1.24 \pm 0.03$ (Fig. 14). In previous studies, this halo was found to be underluminous in both the power-mass correlation at 1.5 GHz and 150 MHz. Together with the relatively flat spectrum and the small size, we suggest that minor mergers can cause the extended radio emission.

Our results show that low-frequency observations are key to observe phenomena producing low-brightness and steep spectrum emission. The presence of multiple HT radio galaxies with extreme lengths suggest that radio galaxies in clusters can enrich the ICM with fossil electrons. Moreover, if the proposed gentle turbulent scenario is a common process for radio galaxies in clusters, then this would imply that large amounts of electrons released into the ICM by AGN would be able to survive with high energies producing a seed population of energetic particles. These seed electrons have been invoked to explain cluster-scale radio emission, such as radio haloes and relics.

DATA AVAILABILITY

Raw data are publicly available in the archives. FITS files of LOFAR HBA can be found at https://lofar-surveys.org/. Processed data used in this work will be made available upon reasonable request.

REFERENCES

Bonafede A. et al., 2022, ApJ, 933, L218
Botteon A. et al., 2018, MNRAS, 478, 885
Botteon A. et al., 2019, A&A, 622, 19
Botteon A. et al., 2020, MNRAS, 499, 11
Botteon A. et al., 2021, A&A, 649, A37
Botteon A. et al., 2022, A&A, 660, A78
Boxelaar J. M., van Weeren R. J., Botteon A., 2021, Astronomy and Computing, 35, 100464
Brunetti G. et al., 2008, Nature, 455, 944
Brunetti G., Jones T. W., 2014, Int. J. Mod. Phys. D, 23, 1430007
Buote D. A., 2001, ApJ, 553, L15
Carilli C. L., Perley R. A., Dreher J. W., Leahy J. P., 1991, ApJ, 383, L554
Cassano R. et al., 2013, ApJ, 777, L141
Cassano R., Brunetti G., 2005, MNRAS, 357, 1313
Cassano R., Brunetti G., Setti G., 2006, MNRAS, 369, 1577
Cassano R., Ettori S., Giacintucci S., Brunetti G., Markevitch M., Venturi T., Gitti M., 2010, ApJ, 721, L82
Cavaliere A., Fusco-Femiano R., 1976, A&A, 49, 137
Chandra P., Ray A., Bhatnagar S., 2004, ApJ, 604, L97
Cuciti V. et al., 2021, A&A, 647, 51
Cuciti V. et al., 2022, Nature, 609, 911
Cuciti V. et al., 2023, A&A, 680, 30
Cuciti V., Brunetti G., van Weeren R., Bonafede A., Dallacasa D., Cassano R., Venturi T., Kale R., 2018, A&A, 609, 61
Cuciti V., Cassano R., Brunetti G., Dallacasa D., Kale R., Ettori S., Venturi T., 2015, A&A, 580, 97
Cutri R. M. et al., 2003, 2MASS All Sky Catalog of point sources
de Gasperin F. et al., 2019, A&A, 622, 5
de Gasperin F. et al., 2020, A&A, 642, 85

de Gasperin F. et al., 2021, A&A, 648, 104
de Gasperin F. et al., 2023, A&A, 673, A165
de Gasperin F., 2017, MNRAS, 467, 2234
de Gasperin F., Ogrean G. A., van Weeren R. J., Dawson W. A., Brüggen M., Bonafede A., Simionescu A., 2015, MNRAS, 448, 2197
De Luca A., Molendi S., 2004, A&A, 419, 837
Duchesne S. W., Johnston-Hollitt M., Bartalucci I., 2021, PASA, 38, e053
Eckert D., Finoguenov A., Ghirardini V., Grandis S., Kaefer F., Sanders J., Ramos-Ceja M., 2020, The Open Journal of Astrophysics, 3, 12
Edler H. W. et al., 2022, A&A, 666, 3
Enßlin T. A., Brüggen M., 2002, MNRAS, 331, 1011
Enßlin T. A., Gopal-Krishna, 2001, A&A, 366, 26
Feretti L., Giovannini G., 2008, in Plionis M., López-Cruz O., Hughes D.eds, Vol. 740, 24, Lecture Notes in Physics, Panchromatic View of Clusters of Galaxies and the Large-Scale Structure, International Advanced School in Inaoe, Tonantzintla-Puebla, Mexico, Springer
Feretti L., Giovannini G., Klein U., Mack K. H., Sijbring L. G., Zech G., 1998, A&A, 331, 475
Garon A. F. et al., 2019, AJ, 157, 126
Giacintucci S. et al., 2022, ApJ, 934, L49
Giacintucci S., Venturi T., Murgia M., Dallacasa D., Athreya R., Bardelli S., Mazzotta P., Saikia D. J., 2007, A&A, 476, 99
Hardcastle M. J. et al., 2021, A&A, 648, 10
Hardcastle M. J., 2013, MNRAS, 433, 3364
Hardcastle M. J., Birkinshaw M., Worrall D. M., 1998, MNRAS, 294, 615
Hardcastle M. J., Croston J. H., 2020, New A Rev., 88, 101539
Harwood J. J., Hardcastle M. J., Croston J. H., Goodger J. L., 2013, MNRAS, 435, 3353
Hill J. M., Longair M. S., 1971, MNRAS, 154, 125
Jaffe W. J., Perola G. C., 1973, A&A, 26, 423
Jones T. W., Nolting C., O'Neill B. J., Mendygral P. J., 2017, Physics of Plasmas, 24, 041402
Kardashev N. S., 1962, Soviet Ast., 6, 317
Katz-Stone D. M., Rudnick L., Anderson M. C., 1993, ApJ, 407, L549
Kempner J. C., Blanton E. L., Clarke T. E., Enßlin T. A., Johnston-Hollitt M., Rudnick L., 2004, in Reiprich T., Kempner J., Soker N.eds, The Riddle of Cooling Flows in Galaxies and Clusters of galaxies. p. 335, preprint (astro-ph/0310263)
Klamer I., Subrahmanyan R., Hunstead R. W., 2004, MNRAS, 351, 101
Kundu S., Vaidya B., Mignone A., 2021, ApJ, 921, L74
Kuntz K. D., Snowden S. L., 2008, A&A, 478, 575
Lal D. V., 2020, AJ, 160, 161
Leccardi A., Molendi S., 2008, A&A, 486, 359
Longair M. S., 2011, High Energy Astrophysics, 3rd edn. Cambridge Univ. Press, Cambridge
Lovisari L. et al., 2017, ApJ, 846, L51
Mandal S. et al., 2019, A&A, 622, 22
Mandal S. et al., 2020, A&A, 634, 4
Mao M. Y., Sharp R., Saikia D. J., Norris R. P., Johnston-Hollitt M., Middelberg E., Lovell J. E. J., 2010, MNRAS, 406, 2578
McMullin J. P., Waters B., Schiebel D., Young W., Golap K., 2007, in Shaw R. A., Hill F., Bell D. J.eds, Vol. 712eds, Vol. 376, Astronomical Data Analysis Software and Systems XVI, Astronomical Society of the Pacific Conference Series, Tucson, Arizona, USA
Migkas K., Schellenberger G., Reiprich T. H., Pacaud F., Ramos-Ceja M. E., Lovisari L., 2020, A&A, 636, 15
Mignone A., Massaglia S., Bodo G., 2004, Ap&SS, 293, 199
Miley G. K., 1973, A&A, 26, 413
Miley G., 1980, ARA&A, 18, 165
Mukherjee D., Bodo G., Rossi P., Mignone A., Vaidya B., 2021, MNRAS, 505, 2267
Müller A. et al., 2021, MNRAS, 508, 5326
Murgia M., Govoni F., Markevitch M., Feretti L., Giovannini G., Taylor G. B., Carretti E., 2009, A&A, 499, 679
Nasa High Energy Astrophysics Science Archive Research Center (Heasarc), 2014, HEAsoft: Unified Release of FTOOLS and XANADU, Astrophysics Source Code Library, record ascl:1408.004

Nolting C., Jones T. W., O'Neill B. J., Mendygral P. J., 2019a, ApJ, 876, L154
Nolting C., Jones T. W., O'Neill B. J., Mendygral P. J., 2019b, ApJ, 885, L80
O'Dea C. P., Owen F. N., 1985, AJ, 90, 927
O'Neill B. J., Jones T. W., Nolting C., Mendygral P. J., 2019a, ApJ, 884, L12
O'Neill B. J., Jones T. W., Nolting C., Mendygral P. J., 2019b, ApJ, 887, L26
Offringa A. R. et al., 2014, MNRAS, 444, 606
Ohmura T., Asano K., Nishiwaki K., Machida M., Sakemi H., 2023, ApJ, 951, 76
Owen F. N., Rudnick L., 1976, ApJ, 205, L1
Pacaud F. et al., 2006, MNRAS, 372, 578
Pacholczyk A. G., 1970, Radio astrophysics. Nonthermal processes in galactic and extragalactic sources
Pal S., Kumari S., 2023, JA&A, 44, 17
Pâris I. et al., 2014, A&A, 563, 54
Parma P., Murgia M., Morganti R., Capetti A., de Ruiter H. R., Fanti R., 1999, A&A, 344, 7
Pasini T. et al., 2022, A&A, 663, 105
Perley R. A., Butler B. J., 2013, ApJS, 204, 19
Pfrommer C., Jones T. W., 2011, ApJ, 730, L22
Planck Collaboration et al., 2016, A&A, 594, 27
Ramos-Ceja M. E., Pacaud F., Reiprich T. H., Migkas K., Lovisari L., Schellenberger G., 2019, A&A, 626, 48
Rossetti M., Gastaldello F., Eckert D., Della Torre M., Pantiri G., Cazzoletti P., Molendi S., 2017, MNRAS, 468, 1917
Rudnick L. et al., 2022, ApJ, 935, L168
Ryle M., Windram M. D., 1968, MNRAS, 138, 1
Sanders J. S. et al., 2016a, MNRAS, 457, 82
Sanders J. S. et al., 2022, A&A, 661, 36
Sanders J. S., Fabian A. C., Russell H. R., Walker S. A., Blundell K. M., 2016b, MNRAS, 460, 1898
Sanders J., Walker S., ZuHone J., Bellomi E., 2018, Chandra News, 25, 1
Sebastian B., Lal D. V., Pramesh Rao A., 2017, AJ, 154, 169
Shimwell T. W. et al., 2017, A&A, 598, 104
Shimwell T. W. et al., 2019, A&A, 622, 1
Shimwell T. W. et al., 2022, A&A, 659, 1
Sijbring D., de Bruyn A. G., 1998, A&A, 331, 901
Smirnov O. M., Tasse C., 2015, MNRAS, 449, 2668
Srivastava S., Singal A. K., 2020, MNRAS, 493, 3811
Stroe A., van Weeren R. J., Intema H. T., Röttgering H. J. A., Brüggen M., Hoeft M., 2013, A&A, 555, 110
Tasse C. et al., 2018, A&A, 611, 87
Tasse C. et al., 2021, A&A, 648, 1
Tribble P. C., 1993, MNRAS, 261, 57
van Haarlem M. P. et al., 2013a, A&A, 556, 2
van Haarlem M. P. et al., 2013b, A&A, 556, 2
van Weeren R. J. et al., 2017, Nature Astron., 1, 0005
van Weeren R. J. et al., 2021, A&A, 651, 115
van Weeren R. J., de Gasperin F., Akamatsu H., Brüggen M., Feretti L., Kang H., Stroe A., Zandanel F., 2019, Space Sci. Rev., 215, 16
van Weeren R. J., Röttgering H. J. A., Brüggen M., 2011, A&A, 527, 114
van Weeren R. J., Röttgering H. J. A., Brüggen M., Cohen A., 2009, A&A, 508, 75
Venkatesan T. C. A., Batuski D. J., Hanisch R. J., Burns J. O., 1994, ApJ, 436, L67
Veronica A. et al., 2022, A&A, 661, 46
Wilber A. et al., 2018, MNRAS, 473, 3536
Wilber A. et al., 2019, A&A, 622, 25
Zhou R. et al., 2021, MNRAS, 501, 3309

APPENDIX A: FDCA RESULTS

FDCA results for the 2D surface brightness fitting to study the central radio halo (see subsection 3.4). The first column refers to the original source-subtracted images shown in Fig. 3.
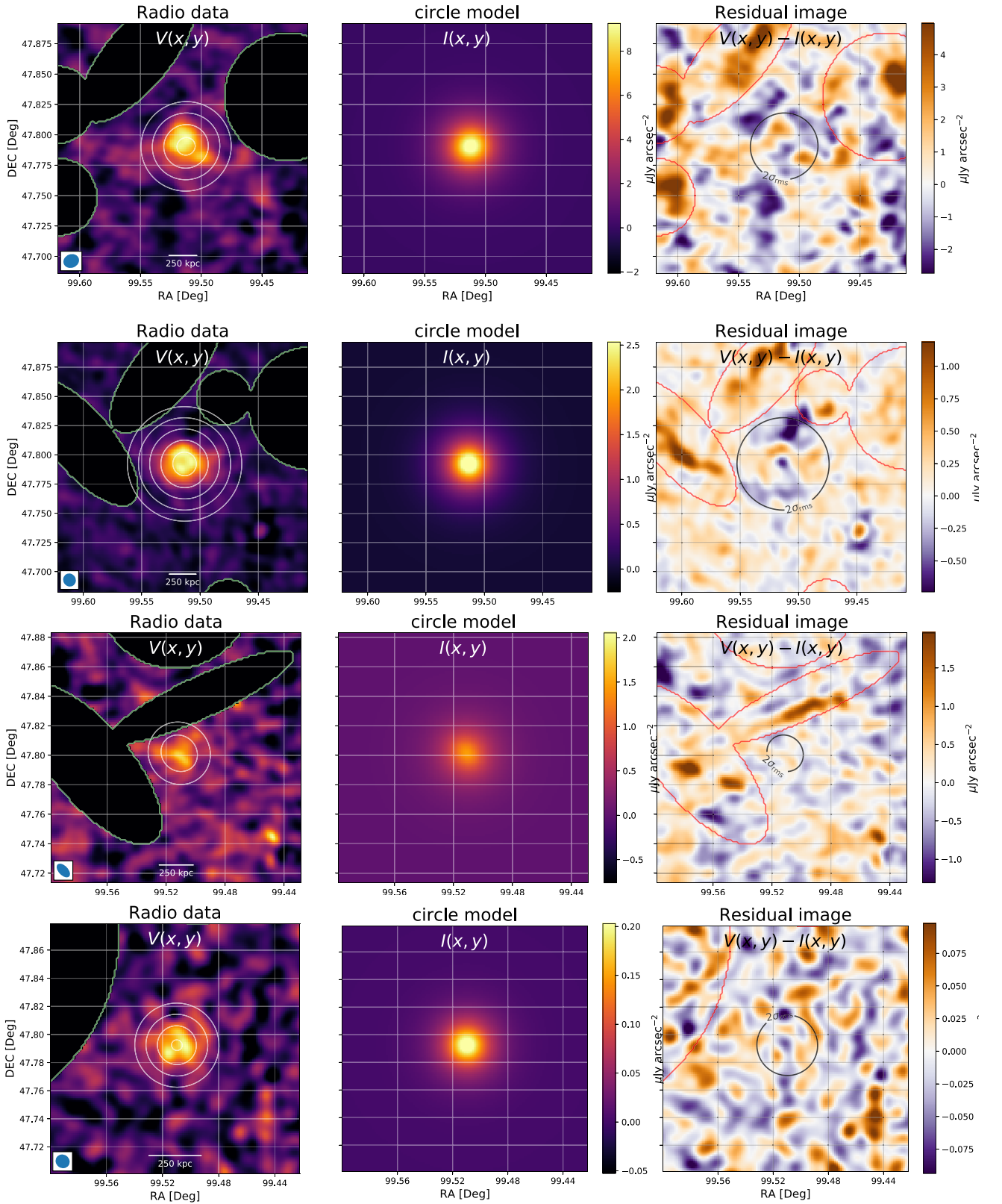
Figure A1. `FDCA-Halo` results for the radio halo in ZwCl 0634.1+4747at LBA (first row), HBA (second row), GMRT (third row), and VLA (fourth row) frequency. Left panel: Original image with the contaminating regions masked out. Middle panel: Circular model map. Right panel: Residual image. The contour shows the $2\sigma_{rms}$ level of the model. The red contours show the masked regions, the contamination sources are visible.

This paper has been typeset from a TEX/LATEX file prepared by the author.